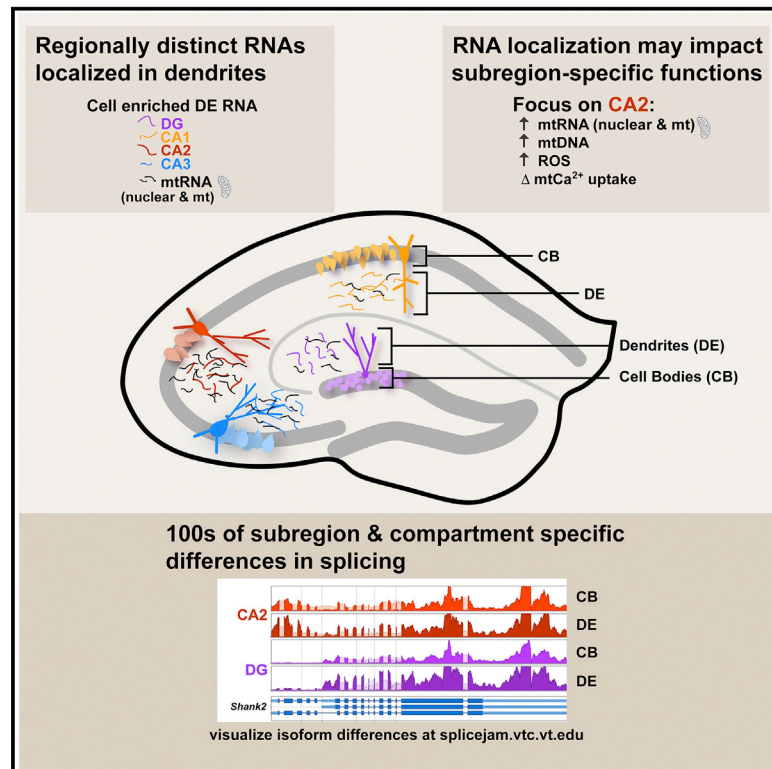


Cell Reports

Hippocampal Subregions Express Distinct Dendritic Transcriptomes that Reveal Differences in Mitochondrial Function in CA2

Graphical Abstract



Authors

Shannon Farris, James M. Ward, Kelly E. Carstens, Mahsa Samadi, Yu Wang, Serena M. Dudek

Correspondence

dudek@niehs.nih.gov

In Brief

RNA localization provides spatial and temporal control over protein expression at synapses. Farris et al. show that hippocampal subregions, areas important for memory, localize distinct subsets of RNAs to dendrites, uncovering an additional layer of cell-specific regulation. Focusing on CA2 dendrites, they identify mitochondria as a regulator of CA2 plasticity.

Highlights

- Each hippocampal subregion expresses a distinct complement of dendritic RNAs
- Splicejam visualizes isoform differences across subregions and compartments
- CA2 is enriched for RNAs encoding proteins involved in mitochondrial function
- Blocking mitochondrial calcium uptake changes plasticity-resistant profile of CA2



Hippocampal Subregions Express Distinct Dendritic Transcriptomes that Reveal Differences in Mitochondrial Function in CA2

Shannon Farris,^{1,4} James M. Ward,² Kelly E. Carstens,¹ Mahsa Samadi,^{1,5} Yu Wang,³ and Serena M. Dudek^{1,6,*}

¹Neurobiology Laboratory, National Institute of Environmental Health Sciences, NIH, Research Triangle Park, NC 27709, USA

²Integrative Bioinformatics, National Institute of Environmental Health Sciences, NIH, Research Triangle Park, NC 27709, USA

³Cellular and Molecular Pathology, National Toxicology Program, NIH, Research Triangle Park, NC 27709, USA

⁴Present address: Center for Neurobiology Research, Fralin Biomedical Research Institute, Virginia Tech Carilion, Roanoke, VA 24016, USA

⁵Present address: Faculty of Medicine Centre, Imperial College London, London, UK

⁶Lead Contact

*Correspondence: dudek@niehs.nih.gov

<https://doi.org/10.1016/j.celrep.2019.08.093>

SUMMARY

RNA localization is one mechanism neurons use to spatially and temporally regulate gene expression at synapses. Here, we test the hypothesis that cells exhibiting distinct forms of synaptic plasticity will have differences in dendritically localized RNAs. Indeed, we discover that each major subregion of the adult mouse hippocampus expresses a unique complement of dendritic RNAs. Specifically, we describe more than 1,000 differentially expressed dendritic RNAs, suggesting that RNA localization and local translation are regulated in a cell type-specific manner. Furthermore, by focusing Gene Ontology analyses on the plasticity-resistant CA2, we identify an enrichment of mitochondria-associated pathways in CA2 cell bodies and dendrites, and we provide functional evidence that these pathways differentially influence plasticity and mitochondrial respiration in CA2. These data indicate that differences in dendritic transcriptomes may regulate cell type-specific properties important for learning and memory and may influence region-specific differences in disease pathology.

INTRODUCTION

As polarized and morphologically complex cells, neurons need to coordinate gene expression patterns across multiple cellular compartments, often hundreds of microns away from the cell soma. To achieve this, neurons localize RNA transcripts to axonal and dendritic compartments to synthesize proteins “on demand” in response to local cues, such as synaptic activity. This process, called local protein synthesis, affords tight spatial and temporal control over gene expression and plays an essential role in the brain throughout development and during learning (Holt and Schuman, 2013; Kiebler et al., 2013; Steward and Schuman, 2001). Given the complexity of neuronal morphology,

it comes as little surprise that dysregulation of RNA localization has been implicated in several neurological diseases, such as fragile X syndrome and other autism spectrum disorders, amyotrophic lateral sclerosis, and Alzheimer’s disease (Donlin-Asp et al., 2017; Holt and Schuman, 2013; Kiebler et al., 2013).

The repertoire of RNA transcripts in adult axons and dendrites *in vivo* and their role(s) during learning and memory are only beginning to be explored. Advancements in RNA sequencing (RNA-seq) technologies have led to the identification of thousands of RNA transcripts in adult hippocampal CA1 dendrites *in vivo* (Ainsley et al., 2014; Cajigas et al., 2012; Nakayama et al., 2017). However, whether different hippocampal cell types express distinct dendritic transcriptomes and whether dendritic RNAs are regulated in a cell type-specific manner are currently unknown. Given that several identified dendritic RNAs have functions at the synapse (Cajigas et al., 2012; Holt and Schuman, 2013), we hypothesized that cell types exhibiting distinct forms of synaptic plasticity might have different complements of dendritically localized RNA. In particular, we were interested in area CA2, a small subregion sandwiched between areas CA1 and CA3 that is known to be resistant to long-term potentiation (LTP) (Zhao et al., 2007) and injury-induced cell death (Nadler et al., 1978), and important for encoding social experience (Pangani et al., 2015; Alexander et al., 2016, 2018; Dudek et al., 2016; Hitti and Siegelbaum, 2014; Raam et al., 2017; Smith et al., 2016; Leroy et al., 2017; Lin et al., 2018; Meira et al., 2018).

To identify uniquely expressed or cell-type-enriched dendritic transcripts, we used laser capture microdissection (LCM) on a transgenic mouse line that expresses enhanced green fluorescence protein (Amigo2-EGFP) in area CA2 cell bodies and dendrites. The EGFP signal in CA2 delineates neighboring subregion borders and enabled the isolation of cell body and dendritic layers from each of the major hippocampal subregions (CA1, CA2, CA3, and dentate gyrus [DG]) for RNA-seq. This revealed more than 1,000 differentially expressed dendritic RNAs, suggesting that local translation plays an important and overlooked layer of cell type-specific regulation in hippocampal neurons *in vivo*. Furthermore, we found that dendritic RNAs display cell type- and compartment-specific patterns of splicing that can be viewed at <http://splicejam.vtc.vt.edu>, although interestingly, we detected



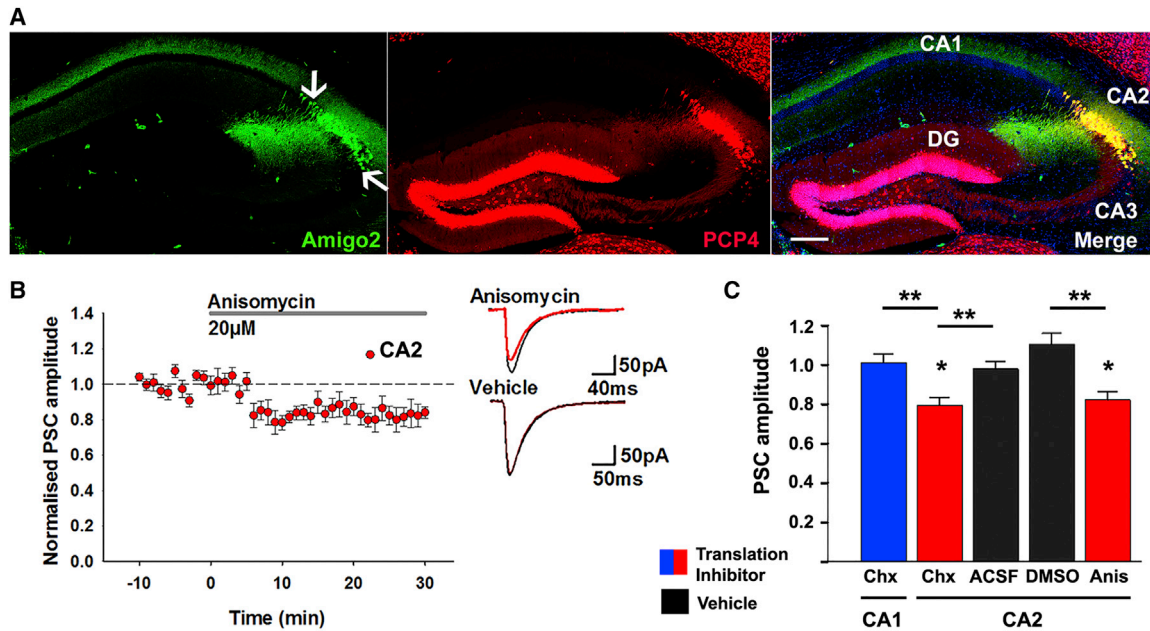


Figure 1. Inhibiting Translation Leads to a Decrease in CA2 Synaptic Responses

(A) Coronal section of an Amigo2-icreERT2; ROSA-tdTomato reporter mouse showing Amigo2 (pseudocolored in green) colocalization with CA2 molecular marker PCP4. Nuclei are counterstained in blue. Arrows denote CA2 borders.

(B) CA2 whole-cell voltage-clamp recordings in acute mouse hippocampal slices in the presence of anisomycin. Gray bar indicates duration of application. Representative traces are shown.

(C) Average amplitudes (\pm SEM) from the last 10 min of recording normalized to baseline for CA1 and CA2 in either cycloheximide (Chx; 60 μ M/ACSF), vehicle conditions (ACSF and DMSO), or anisomycin (Anis; 20 μ M/0.1% DMSO). $n = 6-9$ slices from six to eight mice per condition. ** $p < 0.01$, two-sided t test; * $p < 0.05$ significantly different from baseline.

Scale bar, 250 μ m.

10-fold greater splicing differences across putative interneuron and non-neuronal cells within dendritic laminae. Moreover, we identified an enrichment of RNAs associated with mitochondrial function in CA2 cell bodies and dendrites and show that blocking mitochondrial calcium uptake influences the plasticity-resistant phenotype in CA2 and that CA2 neurons have greater mitochondrial respiration compared with neighboring neurons. In sum, our results support accumulating evidence that thousands of RNAs are present in adult dendrites and extend those findings by identifying more than 1,000 differentially expressed dendritic RNAs in the hippocampus. Furthermore, our data suggest that differences in dendritic transcriptomes regulate cell type-specific properties, such as synaptic plasticity and mitochondrial function, and therefore likely affect learning and memory and region-specific differences in disease pathology.

RESULTS

Ongoing Translation Is Required for Maintaining CA2 Synaptic Transmission

Synapses in the stratum radiatum of area CA2 (Figure 1A) are resistant to LTP, a process that requires local protein synthesis. However, LTP is readily expressed in CA2 neurons from regulator of G-protein signaling 14 (RGS14)-knockout mice (Lee et al., 2010) and can be restored in wild-type mice by inducing LTP in the presence of high external calcium (10 mM; Simons

et al., 2009) or after degradation of perineuronal nets (Carstens et al., 2016). These data indicate that CA2 synapses have the capacity (i.e., cellular machinery) to undergo LTP but suggest that multiple plasticity-restricting mechanisms are at play. In fact, we found that even the maintenance of baseline synaptic transmission in CA2 may require ongoing dendritic protein synthesis, as inhibiting translation with anisomycin or cycloheximide in acutely prepared hippocampal slices leads to a modest but consistent decrease in synaptic responses within 5 min in CA2 neurons but not in CA1 neurons ($p < 0.01$, two-sided t test; $n = 6-9$ slices from six to eight mice per condition; Figures 1B and 1C). Thus, not only synaptic plasticity but also synaptic transmission in CA2 is highly regulated. We hypothesized that local protein synthesis may be setting the threshold for synaptic plasticity at CA2 synapses, which was our motivation for identifying the RNAs enriched in CA2 dendrites.

Identifying Subregion-Specific Dendritic Transcriptomes Using LCM-RNA-Seq

To identify RNAs present in CA2 and neighboring subregion dendrites, we performed RNA-seq on LCM samples captured from the cell body (stratum pyramidale and granule cell layer) or the dendritic laminae (stratum radiatum and molecular layer) from each major subregion in hippocampus (CA1, CA2, CA3, and DG) from three adult male Amigo2-EGFP mice (Figure 2A). We used an optimized low-input LCM-RNA-seq protocol that

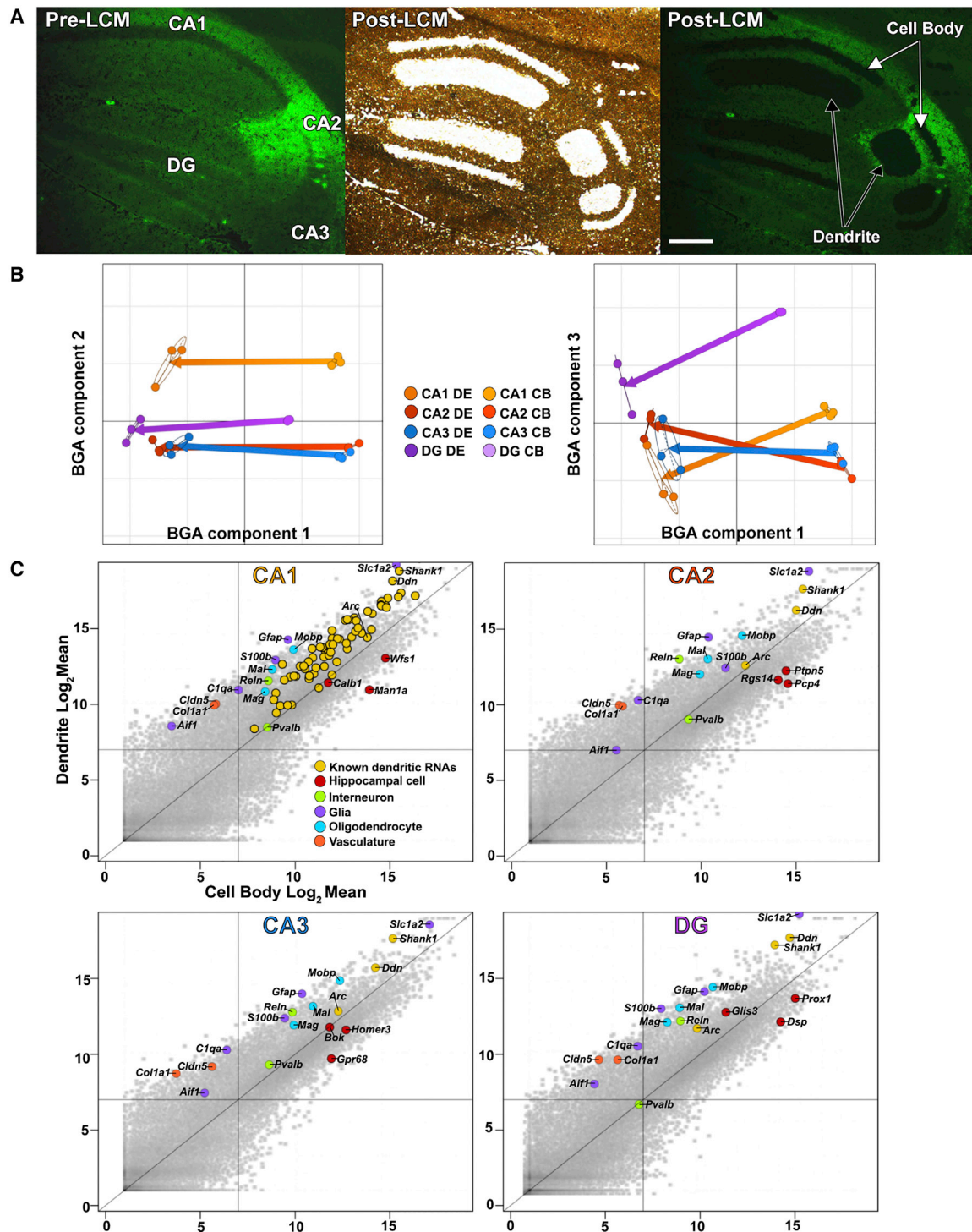


Figure 2. LCM-RNA-Seq to Isolate Subregion-Specific Dendritic Transcriptomes

(A) Sagittal Amigo2-EGFP section pre- (left) and post-laser capture of CA1, CA2, CA3, and DG cell body and apical dendritic compartments in bright field (middle) and fluorescence (right).

(B) Three-dimensional (3D) between-group analysis (BGA) plot of the three biological replicates per cell type (CA1, CA2, CA3, DG) per compartment (cell body, dendrite).

(C) Correlation scatterplots of cell body and dendrite median expression from each subregion. RNAs highlighted in yellow are well-known dendritic RNAs (see Figure S3). Note that non-pyramidal cell markers (interneurons, glia, oligodendrocyte, vasculature) are enriched in the dendrite samples for each subregion. Scale bar, 200 μ m.

obtains considerably higher quality RNA (RNA integrity number [RIN] > 9) and more robust RNA-seq results than current low-input RNA-seq protocols (Farris et al., 2017). RNA-seq data from each of the three biological replicates clustered by cell type and by compartment, as visualized by a between-group analysis (BGA; a method similar to principal-component analysis [PCA] that maximizes distance between sample groups instead of individual samples (Culhane et al., 2002) (Figure 2B). Comparing cell body and dendrite expression within a subregion shows that subregion-specific pyramidal cell markers are enriched in the cell body samples, and non-pyramidal cell markers are enriched in dendrite samples (Figure 2C). The expression of several non-pyramidal cell markers was validated using single-molecule fluorescence *in situ* hybridization (smFISH; Figure S1).

We next evaluated whether the RNAs we detected in our mouse CA1 dendrite samples overlapped with previously published dendritic RNAs isolated from rat CA1, identified using RNA-seq (Cajigas et al., 2012). Out of the 2,550 RNAs identified in rat CA1 dendrites, we detected 2,342 of them (92%) in mouse CA1 dendrites (Figure S2A), suggesting a high degree of conservation in hippocampal dendritic RNAs among rodents. We also compared our mouse CA1 dendritic transcriptome dataset with other recent mouse CA1 dendritic transcriptome datasets acquired using ribosome profiling (Ainsley et al., 2014) or RNA-seq (Nakayama et al., 2017), and similarly, we found a high degree of overlap across datasets. Specifically, 635 RNAs were shared by at least three CA1 dendritic transcriptome datasets, but only 68 RNAs were shared among all four CA1 dendritic transcriptome datasets (Figure S2B). These 68 shared dendritic RNAs are enriched in our CA1 dendrite samples compared with CA1 cell body samples, as seen in Figure 2C.

Area CA2 Transcriptome Is Most Similar to Area CA3 Transcriptome

We found that CA2 cell body and dendrite samples were closest to, but not overlapping with, CA3 cell body and dendrite samples, respectively. Indeed, when data from cell body samples were centered by the mean cell body signal and hierarchically clustered, CA2 and CA3 cell body samples grouped closer together and showed a weak positive correlation with each other (Figure 3A), indicating that these areas have more similar expression profiles with each other than with area CA1 and DG.

Hippocampal Subregions Express Distinct Dendritic Transcriptomes

Next, we assessed whether dendrites express RNAs that are specific to their subregion. We centered the average signal per sample group (e.g., CA2 cell body) by the mean signal per compartment (cell body or dendrite) to compare the deviation from average across sample groups. We measured the degree of correlation between the dendrite and cell body groups across subregions, and remarkably, we found that the dendrite transcriptome from a given subregion strongly correlates with only the cell body transcriptome from the same subregion (Figure 3B).

We saw the same result in an independent LCM pilot experiment comparing gene expression from CA1 and CA2 cell body and dendritic laminae (N = 3 adult male Amigo2-EGFP mice) using whole-transcriptome microarray technology. Namely, we

found that mean subtracted CA1 and CA2 dendrite samples correlated only with their respective cell body samples (Figure S3). These data indicate that each hippocampal subregion expresses a distinct complement of dendritic RNA that is not shared by other hippocampal subregions. Consistent with the cell body data, CA2 and CA3 dendrite samples show a weak positive correlation with CA3 and CA2 cell body samples, respectively, indicating that areas CA2 and CA3 express a subset of shared dendritic RNAs that are not enriched in CA1 and DG dendrites (Figure 3B).

To identify which RNAs drive the positive correlations in Figure 3B, we plotted the cell body differences from the hippocampal mean versus the dendrite differences from the hippocampal mean for each subregion. We identified 1,055 RNAs that showed significant enrichment (defined as >1.5 linear fold change above the mean and a false discovery rate [FDR] of ≤ 0.01) in both the cell body and dendrite sample from any subregion (Figure 3C; Figure S4; Table S1). We classify these RNAs as high-confidence, cell-type-enriched dendritic RNAs. Several high-confidence CA2-enriched dendritic RNAs were validated for dendritic expression using smFISH and immunofluorescence (Figure 3D; Figures S5 and S6).

Cell-Type-Enriched Dendritic RNAs Have Longer 3' UTRs and Are Abundantly Spliced

Importantly, our high-confidence, cell-type-enriched dendritic RNA gene list is an underestimate of the total number of dendritic RNAs expressed in hippocampal neurons, as it excludes dendritic RNAs that are similarly expressed across subregions (e.g., *Camk2a*; Burgin et al., 1990). To address this, we compiled a list of putative dendritic RNAs that are expressed in both cell body and dendrite samples in any subregion well above a noise threshold (Table S2). We reason that a dendritic RNA must be present in the cell body in order to be trafficked to dendrites but that it does not need to be expressed greater in dendrites than in the cell body. This is in contrast to other studies that often define dendritic RNAs as those enriched (e.g., 2-fold greater) in dendrites compared with the cell body. However, as evident in our smFISH images (Figure 3F; Figure S5), there are likely hundreds, if not thousands, of dendritic RNAs that do not fit that profile. Furthermore, requiring cell body expression increases the likelihood that the RNA is from a pyramidal or granule cell source, given that they make up the vast majority of cells within the cell body layers (~95%). In contrast, our dendrite samples contain many classes of cells, including various interneuron populations, astrocytes, microglia, and vasculature endothelial cells, in addition to axons of passage (Cajigas et al., 2012). Thus, our “putative dendritic” RNA list (12,265 RNAs) is inclusive of potential hippocampal dendritic RNAs, but it also contains RNAs that are expressed in additional cell classes present within the dendritic laminae. This may also be true for unvalidated hits in our high-confidence, cell-type-enriched dendritic transcripts. Additionally, we classify two more RNA lists for further analysis: a list of “cell body-retained” RNAs that are expressed in the cell body samples but not the dendrite samples (548 RNAs) and the inverse, a list of putative “non-pyramidal” (or non-granule) cell RNAs that are expressed in the dendrite samples but not the cell body samples (1,871 RNAs) (Figure S7; Table S2). To

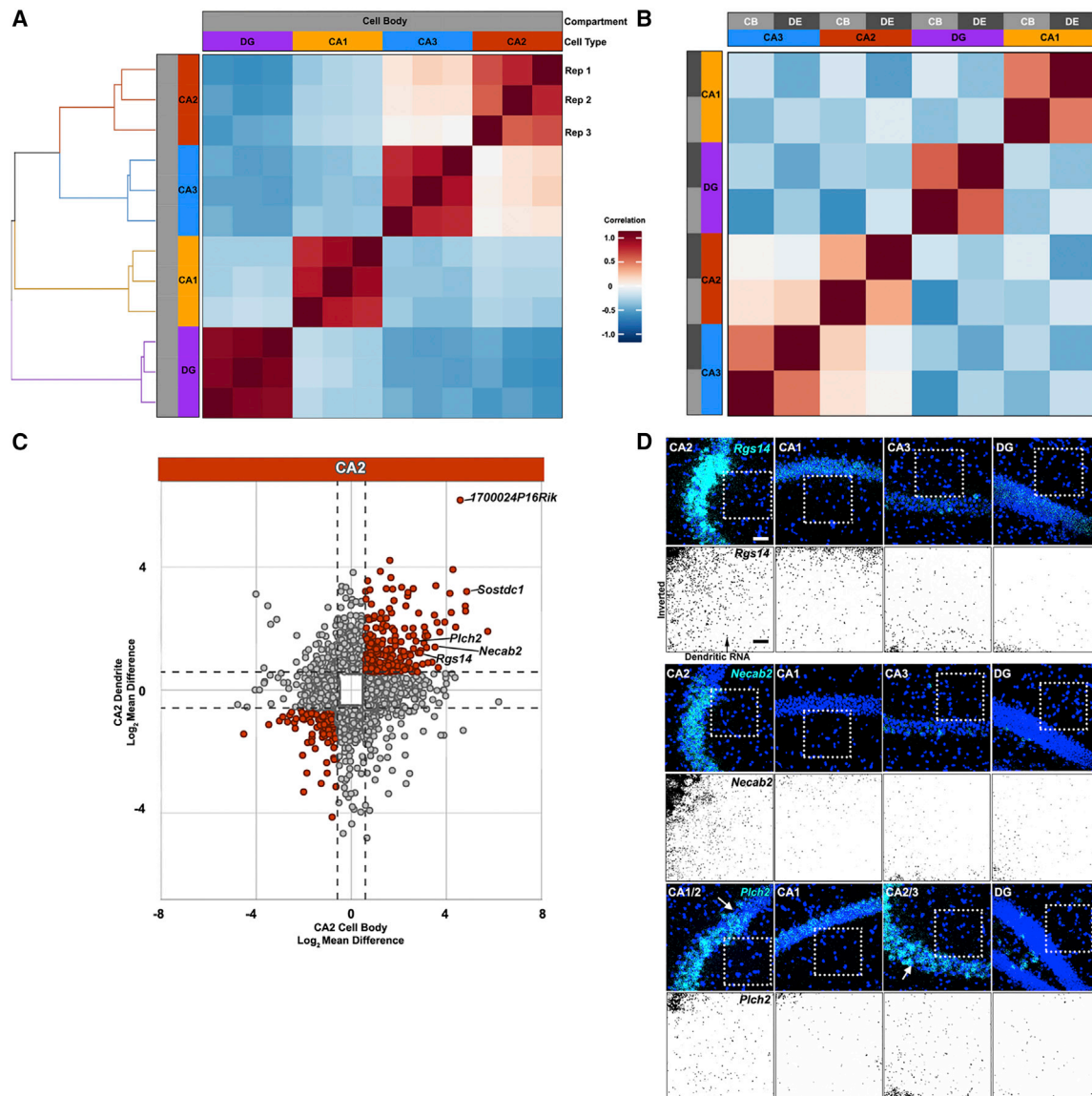


Figure 3. Dendrites from Different Subregions Express Distinct Complements of RNA

(A) Heatmap of cell body correlations for each biological replicate (Rep) centered by the cell body mean. The correlation shows whether the deviation from the mean correlates across replicates. The Euclidean distance is represented by the dendrogram on the left.

(B) Heatmap of average correlations for each cell type centered by the mean per compartment. The correlation shows whether the deviation from the mean correlates across cell body and dendrites. Note that each dendrite sample correlates only with the cell body sample of the same cell type.

(C) Correlation scatterplot of RNAs from CA2 cell body and dendrite samples (from C). RNAs highlighted in red are ± 1.5 -fold change from the mean in both compartments. Labeled and unlabeled RNAs in the upper right quadrant are enriched in both CA2 cell bodies and dendrites compared with the mean across all cell types.

(D) Single-molecule fluorescent *in situ* hybridization (smFISH) confirming that *Rgs14*, *Necab2*, and *Plch2* are enriched in CA2 cell bodies and dendrites compared with CA1, CA3, and DG cell bodies and dendrites. Grayscale inverted images are shown to better visualize dendritic localization. White arrows denote subregion transitions.

Scale bars, 50 and 25 μm . CB, cell body; DE, dendrite.

confirm that the majority of our high-confidence dendritic RNAs are neuronal, we performed hypergeometric enrichment using cell class-specific gene expression to identify cell types overrepresented in each RNA list. Indeed, “neuron” gene expression is statistically overrepresented in the high-confidence dendrite and cell-body-retained lists but not in the non-pyramidal RNA list.

“Microglia” and “astrocyte” gene expression are statistically overrepresented in the non-pyramidal list but not in the high-confidence dendrite and cell-body-retained lists (Figure S7).

With these lists, we sought to determine whether RNA sequence properties that have been previously described for dendritic transcriptomes were also evident in our candidate

dendritic RNAs. A recent study using mouse cortical synaptoneuroosomes found synaptically localized mRNAs have longer 3' UTRs (Ouwenga et al., 2017). In agreement, another recent study using 3'-end sequencing to identify 3' UTRs of dendritically localized RNAs in CA1 also found them to be significantly longer than non-localized RNAs, but they also found this to be true of somatically enriched RNAs (Tushev et al., 2018). When assessing the types of transcripts present in each RNA list, we found that the putative dendritic and high-confidence, cell-type-enriched dendritic transcripts had a greater proportion of protein coding transcripts harboring 3' UTRs compared with cell body-retained, non-pyramidal, or all detected protein coding transcripts (putative dendritic 74.4%, high-confidence dendritic 65.8%, cell body retained 38.0%, non-pyramidal 53.0%, all detected protein coding transcripts 65.7%; Figure S7). Furthermore, using GENCODE-annotated 3' UTR lengths per transcript, we compared the average 3' UTR length of detected transcripts across RNA lists. Consistent with previous studies, high-confidence, cell-type-enriched dendritic RNAs showed significantly longer 3' UTRs compared with the cell body-retained transcripts ($p = 2.41 \times 10^{-29}$) and the non-pyramidal transcripts ($p = 2.59 \times 10^{-8}$, Wilcoxon rank-sum test with continuity correction; Figure S7).

The non-pyramidal transcripts also showed statistically longer 3' UTRs compared with the cell body-retained transcripts ($p = 1.25 \times 10^{-17}$, Wilcoxon rank-sum test with continuity correction), suggesting that the effect may in part be driven by shorter 3' UTRs in the cell body-retained RNAs (Figure S7). Strikingly similar results were obtained using the observed 3' UTR lengths and gene-level 3' UTR lengths (data not shown).

Another recent study using developing cortical neurons in culture found that neurite-localized mRNAs preferentially express distal alternative last exons (ALEs) (Taliaferro et al., 2016), but this was not seen for localized RNAs in mature hippocampal CA1 neurons *in vivo* (Tushev et al., 2018). In order to determine whether our hippocampal dendritic RNAs preferentially express ALEs, we identified GENCODE-annotated transcripts with ALE isoforms but found that because of overlapping last exons, many transcripts could not be distinctly classified. Instead, we classified proximal and distal 3' UTRs using differential 3' UTR start sites and compared isoform-specific expression (in transcripts per million [TPM]) for transcripts with RNA-seq signal spanning a proximal and a distal 3' UTR. We found a general bias toward higher expression for the distal 3' UTR in all our RNA lists (Figure S7), suggesting that distal 3' UTR expression is a neuron-wide phenomenon, independent of localization. These data are consistent with those of Taliaferro et al. (2016) in that they also reported an increase in distal ALE expression with neuronal differentiation in Cath.a-differentiated (CAD) and human neural precursor (NPC) cells.

We were also interested in knowing whether codon use, as a proxy for optimal translation, was different in dendritically localized RNAs compared with RNA retained in cell bodies or from non-pyramidal neurons. To test this, we used the codon adaptation index (CAI), which measures the deviation of a given coding sequence from a reference set (Nakamura et al., 2000; Sharp and Li, 1987). Because average CAI per transcript positively correlates with coding sequence (CDS) length (the longer the tran-

script, the less rare codons affect average CAI), we compared the percentage of low-CAI codons ($CAI \leq 0.5$) per detected transcript for each RNA list. We found that our high-confidence, cell-type-enriched dendritic transcripts showed significantly fewer percentage of low-CAI codons per transcript compared with the cell body-retained RNAs ($p = 2.23 \times 10^{-25}$, Wilcoxon rank-sum test with continuity correction) and non-pyramidal RNAs ($p = 1.46 \times 10^{-8}$, Wilcoxon rank-sum test with continuity correction; Figure S7), suggesting that dendritic transcripts have slightly more optimal CDS, although the differences we detected across RNA lists were small (cell-type-enriched dendritic transcripts 9.74% low-CAI codons per transcript versus cell body-retained transcripts 10.9% and non-pyramidal transcripts 10.2% low-CAI codons per transcript).

When comparing isoform-specific expression across all detected transcripts, we identified thousands of differentially spliced isoforms across cell types and compartments (3,298 differentially spliced transcript isoforms from 2,111 unique genes across all comparisons; hits were defined as having a linear fold change ≥ 1.5 and an adjusted p value of ≤ 0.05 ; Table S3). Interestingly, only a minor percentage of isoform hits came from cell body comparisons (e.g., CA1 cell body versus CA2 cell body, 191 differentially spliced transcript isoforms from 119 unique genes), suggesting that mature hippocampal neurons overwhelmingly express the same isoforms in similar proportions for co-expressed genes, albeit with nearly 200 exceptions. In contrast, the vast majority of differentially expressed isoform hits came from dendrite comparisons (3,137 differentially spliced transcript isoforms from 2,037 unique genes). A subset of these hits overlapped with the two-way comparison (e.g., CA2 cell body to dendrite versus CA1 cell body to dendrite, 373 differentially spliced transcript isoforms from 281 unique genes), suggesting either cell-type and/or compartment-specific splicing.

Next, we further investigated specific examples of subregion and/or compartment-specific differential isoform expression. The known dendritic RNA encoding the α -amino-3-hydroxy-5-methyl-4-isoxazolepropionic acid (AMPA) receptor 1, *Gria1* (Grooms et al., 2006; Ju et al., 2004), has two isoforms that differ by mutually exclusive exons within the coding region, termed flip and flop isoforms (Sommer et al., 1990). As previously demonstrated for cell body expression (Sommer et al., 1990), CA1 and DG cell bodies express both isoforms, with the flop isoform being more abundant, whereas areas CA2 and CA3 cell bodies express predominantly the flip isoform (CA2 CB versus CA1 CB, \log_2 FC = 2.5, $p = 1.20 \times 10^{-10}$; CA2 CB versus DG CB, \log_2 FC = 2.0, $p = 7.54 \times 10^{-7}$; Figures 4A and 4B). Interestingly, these isoform preferences were not maintained in dendrites, as both isoforms were detected in all subregion dendrites at similar ratios, albeit at lower levels (CA2 DE versus CA1 DE, $p > 0.05$; CA2 DE versus DG DE, $p > 0.05$; Figure 4B).

As an example of cell-specific dendritic RNA splicing, we found that *Shank2* RNA is found predominantly expressed as two isoforms that differ in their 5' sequences, the longer of which is statistically more abundant in CA1 and CA2 cell bodies and dendrites compared with the shorter isoform that is more abundant in CA3 and DG cell bodies and dendrites (CA2 CB versus DG CB, \log_2 FC = 6.8, $p = 3.08 \times 10^{-4}$; CA2 DE versus DG DE, \log_2 FC = 5.8, $p = 1.81 \times 10^{-6}$; Figures 4C and 4D). Both

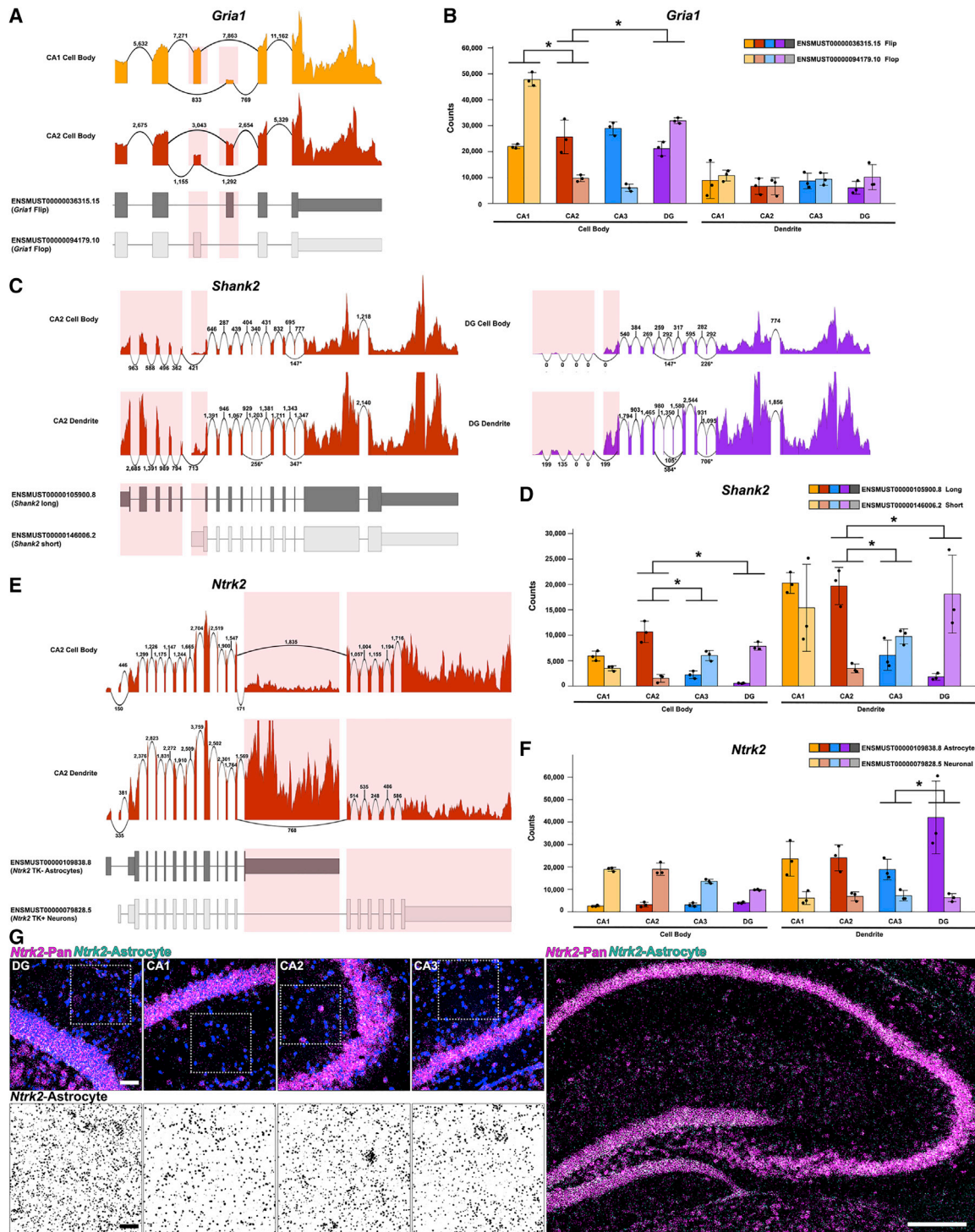


Figure 4. Subregion- and Compartment-Specific Splicing of Hippocampal RNAs

(A) *Gria1* isoform-specific sashimi plots for CA1 and CA2 cell body samples visualizing the summed counts per exon from three replicates with the arcs representing the summed number of junction spanning reads.

(B) *Gria1* bar plot for all groups (CA2CB versus CA1CB, \log_2 FC = 2.5, $p = 1.20 \times 10^{-10}$; CA2CB versus DGCB, \log_2 FC = 2.0, $p = 7.54 \times 10^{-7}$; CA2DE versus CA1DE, $p > 0.5$; CA2DE versus DGDE, $p > 0.5$).

(C) *Shank2* isoform-specific sashimi plots for CA2 and DG cell body and dendrite samples.

(legend continued on next page)

Shank2 isoforms are more abundant in dendrites compared with cell bodies, but the dendritic isoforms are found at levels proportional to their respective cell body levels (Figure 4D). These findings are suggestive of active dendritic targeting that is consistent with previous studies on *Shank* RNA localization in rat CA1 (Epstein et al., 2013).

As discussed above, we detected more than 10-fold more splicing events in dendrite comparisons (i.e., CA1 dendrites versus CA2 dendrites; Table S3) compared with cell body comparisons, suggesting that differential isoform expression in the adult hippocampus may be driven predominantly by different classes of cells (i.e., interneurons or astrocytes), as opposed to subregion- or compartment-specific expression. One example is the brain-derived neurotrophic factor (BDNF) receptor *Ntrk2* (also known as TrkB), of which we detected two major isoforms in each compartment (Figures 4E and 4F). The cell body samples predominantly expressed the full-length, catalytically active *Ntrk2* isoform (referred to as TK+) and the dendrite samples predominantly expressed a truncated *Ntrk2* isoform that lacks tyrosine kinase activity (referred to as TK-) (Middlemas et al., 1991) and is thought to be solely expressed by astrocytes (Rose et al., 2003). We determined the level of neuron versus astrocyte *Ntrk2* in dendrites by comparing the isoform-specific counts and found no differences in neuronal *Ntrk2* across subregions. However, we did find that astrocyte *Ntrk2* in DG dendrites was greater compared with that found in CA3 dendrites (DG DE versus CA3 DE, \log_2 FC = 1.3, $p = 5.43 \times 10^{-3}$; Figure 4F). We validated this finding using isoform-specific smFISH and found that indeed DG dendrites expressed more astrocyte-*Ntrk2* compared with neighboring subregion dendrites (Figure 4G). We also detected the astrocyte-*Ntrk2* specific probe in all subregion cell bodies, suggesting that, at least in the hippocampus, pyramidal neurons express both *Ntrk2* isoforms and the astrocyte-*Ntrk2* expressed in dendrites appears to come from both pyramidal and non-pyramidal cell expression.

Mitochondrial Pathways Are Overrepresented in CA2 Cell Bodies and Dendrites

Next, in order to determine whether differences in RNA might reveal functional differences between subregions, we performed Gene Ontology analyses on differentially expressed RNAs from comparisons with CA2. We limited our analyses to RNAs expressed above a high threshold ($>9 \log_2$ counts) in at least one cell body sample to enrich for genes of neuronal origin and performed hypergeometric enrichment analyses on comparisons between CA2 cell body and dendrite samples to neighboring subregion cell body and dendrite samples, respectively, to identify gene ontologies over- and under-represented in each comparison. To easily visualize the gene ontologies enriched in two

or more comparisons, we hierarchically clustered the top 10 enrichment p values from each comparison, which we clustered into 10 groups by similar enrichment (Figure 5A; Tables S4 and S5).

As expected for hippocampal neurons, the gene ontologies in the top cluster represented neuronal systems and synaptic transmission, and they were significant in CA2 cell body and dendrite-enriched comparisons (up), as well as CA2 cell body and dendrite-depleted comparisons (down; and thus enriched in DG, CA1, and CA3 cell body and dendrite samples) (Figure 5B). Unexpectedly, multiple mitochondrial pathways were present in the cluster representing pathways enriched in CA2 cell body and dendrite comparisons but not enriched in DG, CA1, or CA3 cell body and dendrite comparisons (cluster 3, Figure 5B), suggesting that mitochondrial function might be different in CA2. A subset of gene ontologies is visualized in a gene-concept network in Figure 5C, showing RNAs with significant enrichment in three or more CA2 cell body and/or dendrite comparisons.

Mitochondrial Calcium Uniporter RNA Is Highest in CA2 and Regulates Synaptic Plasticity

Consistent with the Gene Ontology data, mitochondrial genes that regulate mitochondrial calcium signaling were enriched in CA2 and include the mitochondrial calcium uniporter (*Mcu*) and its calcium-sensing regulatory protein *Micu1* (Figure 6A). Both *Mcu* and *Micu1* were present in dendrite samples and validated with smFISH (Figure 6B). One of the strengths of smFISH is the ability to accurately quantify the number of RNA molecules in a given region. Our RNA-seq and smFISH counts were in strong agreement for those tested, including *Mcu* (Figure 6C).

Previous studies have reported that mitochondrial RNAs are present in axons and dendrites (Aschrafi et al., 2016; Lein et al., 2007; Shigeoka et al., 2016; Yoon et al., 2012), but their potential role(s) in synaptic plasticity in dendrites have not been explored. Recent studies have shown that the stoichiometric ratio of MICU1 to MCU dictates the amount of calcium uptake into mitochondria in various tissues, including the heart and liver (Paillard et al., 2017). With both smFISH and RNA-seq data, we find that CA2 neurons have the lowest *Micu1*-to-*Mcu* ratio compared with neighboring subregions (Figure 6D), suggesting that CA2 neurons might have more mitochondrial calcium uptake. Given the important role of calcium in inducing synaptic plasticity, and previous data showing calcium buffering and extrusion are 4 times greater in area CA2 dendrites and spines compared with area CA1 dendrites and spines (Simons et al., 2009), we hypothesized that greater mitochondria calcium influx in CA2 may be contributing to the robust calcium handling in CA2 neurons that is known to restrict plasticity there (Simons et al., 2009). Indeed, we found that inhibiting mitochondrial calcium

(D) *Shank2* bar plot (CA2CB versus DGCB, \log_2 FC = 6.8, $p = 3.08 \times 10^{-4}$; CA2CB versus CA3CB, \log_2 FC = 4.5, $p = 1.27 \times 10^{-3}$; CA2DE versus DGDE, \log_2 FC = 5.8, $p = 1.81 \times 10^{-6}$; CA2DE versus CA3DE, \log_2 FC = 3.2, $p = 5.26 \times 10^{-5}$).

(E) *Ntrk2* isoform-specific sashimi plots for CA2 cell body and dendrite samples.

(F) *Ntrk2* bar plot (DGDE versus CA3DE, \log_2 FC = 1.3, $p = 5.43 \times 10^{-3}$).

(G) Confocal images of isoform-specific *Ntrk2* smFISH in each subregion. *Ntrk2*-pan (magenta) detects both isoforms and *Ntrk2*-astrocyte (cyan) detects only the shorter TK- isoform. Grayscale inverted images are shown to better visualize *Ntrk2*-astrocyte dendritic expression. Note that co-localization of the two probes appears white, and the signal in the cell body layers indicates that both isoforms are expressed in hippocampal neurons.

Scale bars, 50 and 250 μ m. Error bars represent \pm SD. * $p < 0.01$. For full statistics, see Table S3.

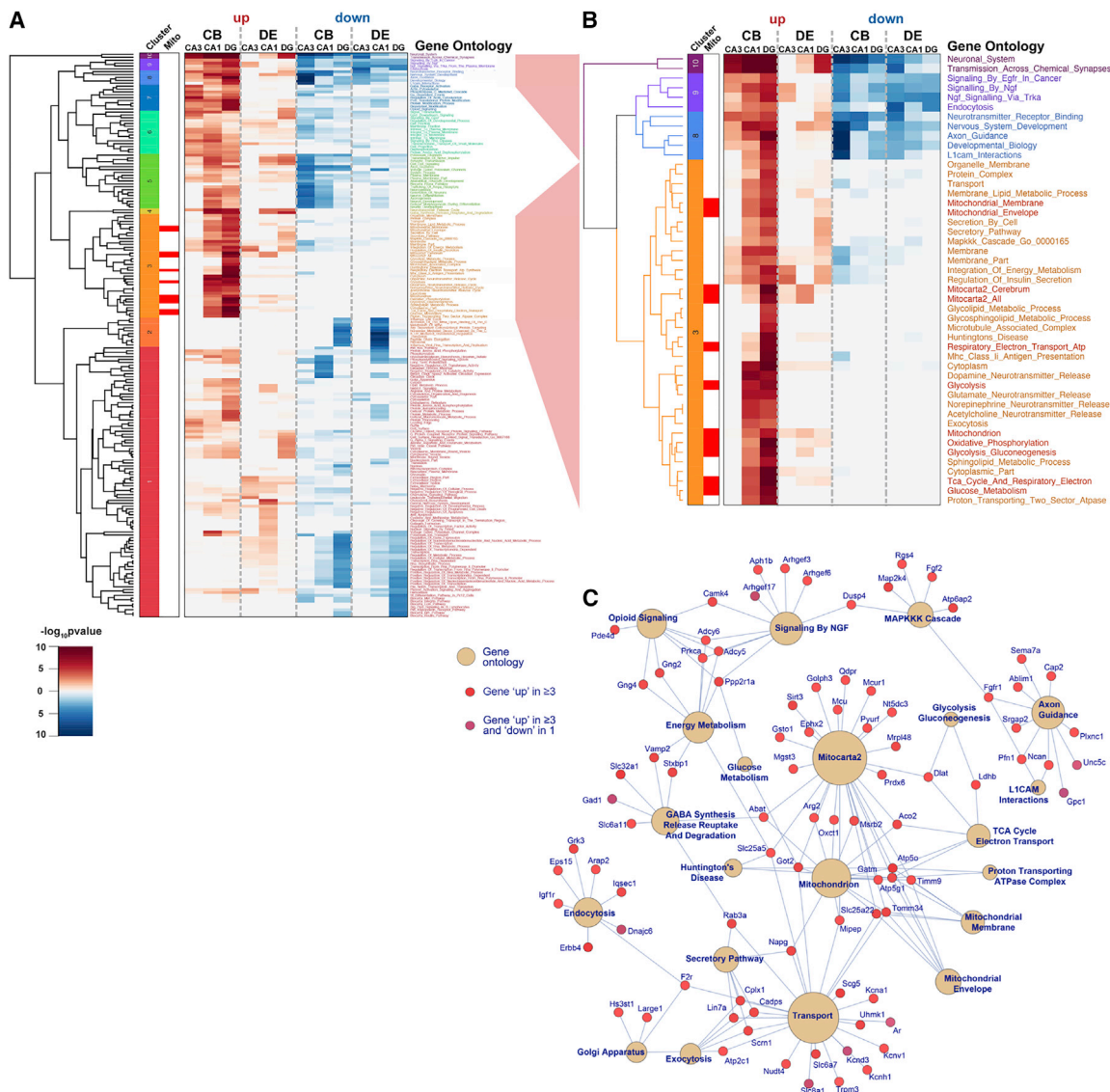


Figure 5. Genes Involved in Mitochondrial Function Are Overrepresented in CA2 Cell Bodies and Dendrites

(A) Heatmap of Gene Ontology p values for each cell body and dendrite comparison with CA2, clustered by similarity. p values shaded in red are enriched in CA2 (up), and p values in blue are depleted in CA2 (down) and therefore enriched in the other cell type. See Table S5 for full statistics.

(B) Zoom in of clusters 3, 8, 9, and 10 from (A). Mitochondrial gene ontologies with enrichment in two or more “up” comparisons but no enrichment in “down” comparisons are denoted in red.

(C) Cnet plot made with a subset of gene ontologies from (B) with two or more genes statistically enriched in three or more CA2 “up” comparisons.

uptake by MCU with Ru360 (10 μ M) permitted long-term depression in CA2 neurons when given an LTP pairing protocol that typically has no effect on CA2 post-synaptic currents (PSCs) (Ru360-LTP = 42% \pm 11% of baseline PSC amplitude, Ru360-no LTP = 82% \pm 13% of baseline PSC amplitude; p = 0.039, two-tailed t test; Figures 6E and 6F), suggesting that mitochondrial calcium uptake is changing the way synaptic calcium levels are influencing plasticity in CA2.

We found no statistically significant difference in CA2 baseline synaptic responses when mitochondrial calcium uptake was blocked by Ru360 (Figures 6G and 6H). However, in CA1 we found a short-term enhancement of baseline synaptic responses

when mitochondrial calcium uptake was blocked by Ru360 (p = 0.0457, two-tailed t test; CA2 Ru360, 84% \pm 14%; CA1 Ru360, 137% \pm 19%; Figures 6G and 6H), indicating that mitochondrial calcium uptake differs between subregions.

CA2 Neurons Have Greater mtDNA Content and Mitochondrial Respiration

In addition to the enrichment of nuclear-encoded mitochondrial genes in CA2, we found that CA2 cell body samples had the most RNA-seq reads that mapped to mtDNA (or chromosome M) (compartment p < 0.0001, cell type p = 0.0022, interaction p = 0.0297; CB: CA2 versus CA1, p = 0.0017; CA2 versus CA3,

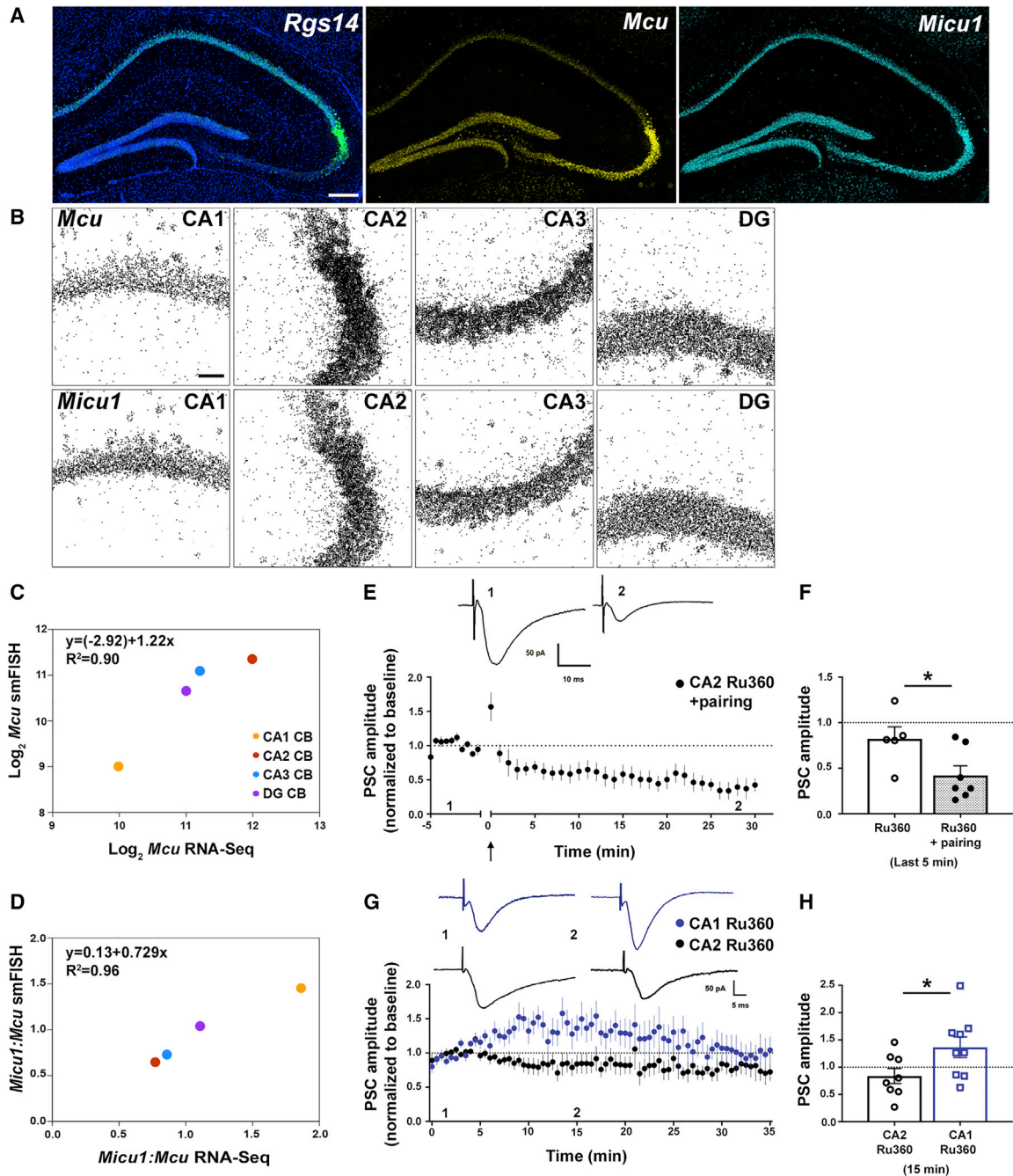


Figure 6. Mitochondrial Calcium Uptake Regulates Synaptic Plasticity in CA2

(A) smFISH images of *Rgs14* (CA2 marker), *Mcu* and *Micu1* mRNA in the mouse hippocampus. The nuclear marker DAPI is counterstained in blue.

(B) Grayscale inverted images of *Mcu* and *Micu1* in each subregion to visualize expression in dendrites.

(C) Correlation of smFISH and RNA-seq values for *Mcu* expression.

(D) Correlation of smFISH and RNA-seq *Micu1:Mcu* ratios. A recent study suggests that the lower the ratio, the greater mitochondria calcium influx (Paillard et al. 2017).

(E) Whole-cell voltage-clamp recordings from CA2 neurons in acute mouse hippocampal slices. PSCs in CA2 are normally unchanged in response to an LTP “pairing protocol” (denoted by black arrow; see STAR Methods), however, with MCU blocker Ru360 (10 μ m) in the patch pipette, the protocol results in synaptic depression. Representative traces at the time points indicated are shown.

(F) Average amplitudes (\pm SEM) from the last 5 min of recording normalized to baseline (* p = 0.039, two-tailed t test; Ru360, $82 \pm 13\%$, n = 5 cells from four mice; Ru360 + pairing, $42 \pm 11\%$, n = 7 cells from five mice).

(legend continued on next page)

$p = 0.2934$; CA2 versus DG, $p = 0.0020$; two-way ANOVA with Dunnett's post hoc tests; $N = 3$; Figure 7A). We did not detect any differences among dendrite samples, however (DE: CA2 versus CA1, $p = 0.9843$; CA2 versus CA3, $p = 0.1810$; CA2 versus DG, $p = 0.0703$; two-way ANOVA with Dunnett's post hoc tests; $N = 3$; Figure 7A). These data suggest that either CA2 neurons have greater levels of mtDNA transcription or a greater amount of mtDNA. To determine whether CA2 neurons have a greater number of mtDNA copies per cell compared with neighboring subregions, we performed LCM and extracted genomic DNA for qPCR. Indeed, we found that CA2 and CA3 neurons had more than twice the amount of mtDNA per cell (normalized to *ActB* DNA) compared with CA1 and DG neurons (compartment $p < 0.0001$, cell type $p < 0.0001$, interaction $p < 0.0001$; CB: CA2 versus CA1, $p = 0.0001$; CA2 versus CA3, $p = 0.4828$; CA2 versus DG, $p = 0.0001$; two-way ANOVA with Dunnett's post hoc tests; $N = 3$; Figure 7B). Again, we did not detect any differences among dendrite samples (DE: CA2 versus CA1, $p = 0.9583$; CA2 versus CA3, $p = 0.9229$; CA2 versus DG, $p = 0.1581$; two-way ANOVA with Dunnett's post hoc tests; $N = 3$; Figure 7B). To visualize this difference, we also performed smFISH to detect mtDNA, which is possible because of the plasmid-like form of mtDNA. We detected a similar 2-fold greater mtDNA content in CA2 and CA3 neurons compared with CA1 and DG neurons (compartment $p < 0.0001$, cell type $p < 0.0001$, interaction $p < 0.0015$; CB: CA2 versus CA1, $p = 0.0007$; CA2 versus CA3, $p = 0.8456$; CA2 versus DG, $p = 0.0001$; two-way ANOVA with Dunnett's post hoc tests; $N = 4$; Figures 7C and 7D). Interestingly, in contrast to what we found using qPCR, smFISH revealed a significantly lower amount of mtDNA in CA1 dendrites, compared with neighboring subregions (DE: CA2 versus CA1, $p = 0.0018$; CA2 versus CA3, $p = 0.6867$; CA2 versus DG, $p = 0.8604$; two-way ANOVA with Dunnett's post hoc tests; $N = 4$).

In order to visualize mitochondria in CA2 neurons, we performed immunohistochemistry using enzymes known to localize to mitochondria, including the citric acid cycle (TCA) enzyme pyruvate dehydrogenase (PDH) and the electron transport chain (ETC) enzyme cytochrome c oxidase IV (COXIV). We found that staining for PDH (Figure 7E) and COXIV (Figure S5) was most robust in CA2 and CA3 neurons. However, we did not detect any qualitative differences in mitochondrial appearance at the level of electron microscopy between areas CA1 and CA2 (data not shown). Interestingly, PDH and COXIV are both important in the generation of energy, and their enzymatic activities are positively regulated by mitochondrial calcium (Llorente-Folch et al., 2015; McCormack et al., 1990).

In fact, several enzymes within the TCA cycle were enriched in CA2 (e.g., *Aldh2*, *Aco2*, *Ldhd*, *Dlat*, *Pdha1*, *Pdk2*, *Sdh*, *Ogdh*, *Cs*, *Atp5g1*; Figure 4C), and when coupled with the fact that the 13 proteins encoded within mtDNA are all involved in oxidative phosphorylation, we hypothesized that mitochondria in CA2

neurons might be producing energy at a higher rate than neighboring subregions. To test this, we measured superoxide production in each subregion using dihydroethidium (DHE) labeling. In otherwise untreated mice, we found that CA2 neurons had the highest level of DHE labeling, indicating that they produce the most superoxide, consistent with greater levels of mitochondrial respiration (overall effect of cell type, $p = 0.0005$; CA2 versus CA1, $p = 0.0038$; CA2 versus CA3, $p = 0.0023$; CA2 versus DG, $p = 0.5723$; paired one-way ANOVA with Geisser-Greenhouse correction and Dunnett's post hoc tests; $N = 5$; Figures 7F and 7G).

DISCUSSION

We sought to determine whether different hippocampal subregions localize distinct subsets of dendritic RNAs that would reflect their unique forms of plasticity and diverse functions underlying learning and memory. To test this, we generated hippocampal subregion- and compartment-specific transcriptomes with stranded, paired-end reads of sufficient depth to perform robust differential gene and isoform analyses. We found that each hippocampal subregion expresses a unique complement of dendritic RNAs that is distinct compared with neighboring subregions. We created a web resource (<http://splicejam.vtc.vt.edu>) for the community to visualize and mine these differences across hippocampal cell types and compartments. By focusing our analyses on CA2, we discovered unforeseen differences in mitochondrial calcium handling and respiration as being important for CA2 plasticity and function. We anticipate that this dataset will continue to provide insights regarding cell type-specific regulation in the hippocampus for the field to explore.

Inhibiting Translation Decreases CA2 Synaptic Responses within Minutes

Local translation of plasticity-related proteins has been shown to be required for many forms of plasticity and long-term memory formation (Kandel et al., 2014). Typically, application of translation inhibitors has no effect on baseline synaptic responses in the hippocampus. However, their effects become evident only after LTP induction, when the potentiation slowly decays back to baseline. The extent of blockade and which phase of LTP is affected seems to be synapse-dependent (Abraham and Williams, 2008; Hagena and Manahan-Vaughan, 2013). Thus, we were surprised to find that blocking translation led to a decrease in baseline synaptic responses in CA2 neurons. We saw the same effect using two different inhibitors, anisomycin and cycloheximide, which differ in their modes of action, and the effect was seen within 5 min, suggesting that the effect was not due to a loss of protein being trafficked from the cell soma. Thus, the decrease in synaptic responses in CA2 most likely was due to a loss of ongoing *de novo* local translation. Future studies are needed to identify (the lack of) which protein(s) caused this

(G) Whole-cell voltage-clamp recordings from CA1 and CA2 neurons in acute mouse hippocampal slices with MCU blocker Ru360 (10 μm) in the patch pipette. Representative traces at the time points indicated are shown.

(H) Average PSC amplitudes (\pm SEM) from CA2 and CA1 at the 15 min time point normalized to baseline ($*p = 0.0457$, two-tailed t test; CA2 Ru360, $84 \pm 14\%$, $n = 8$ cells from five mice; CA1 Ru360, $137 \pm 19\%$, $n = 9$ cells from five mice).

Scale bars, 250 and 50 μm . PSC, post-synaptic current.

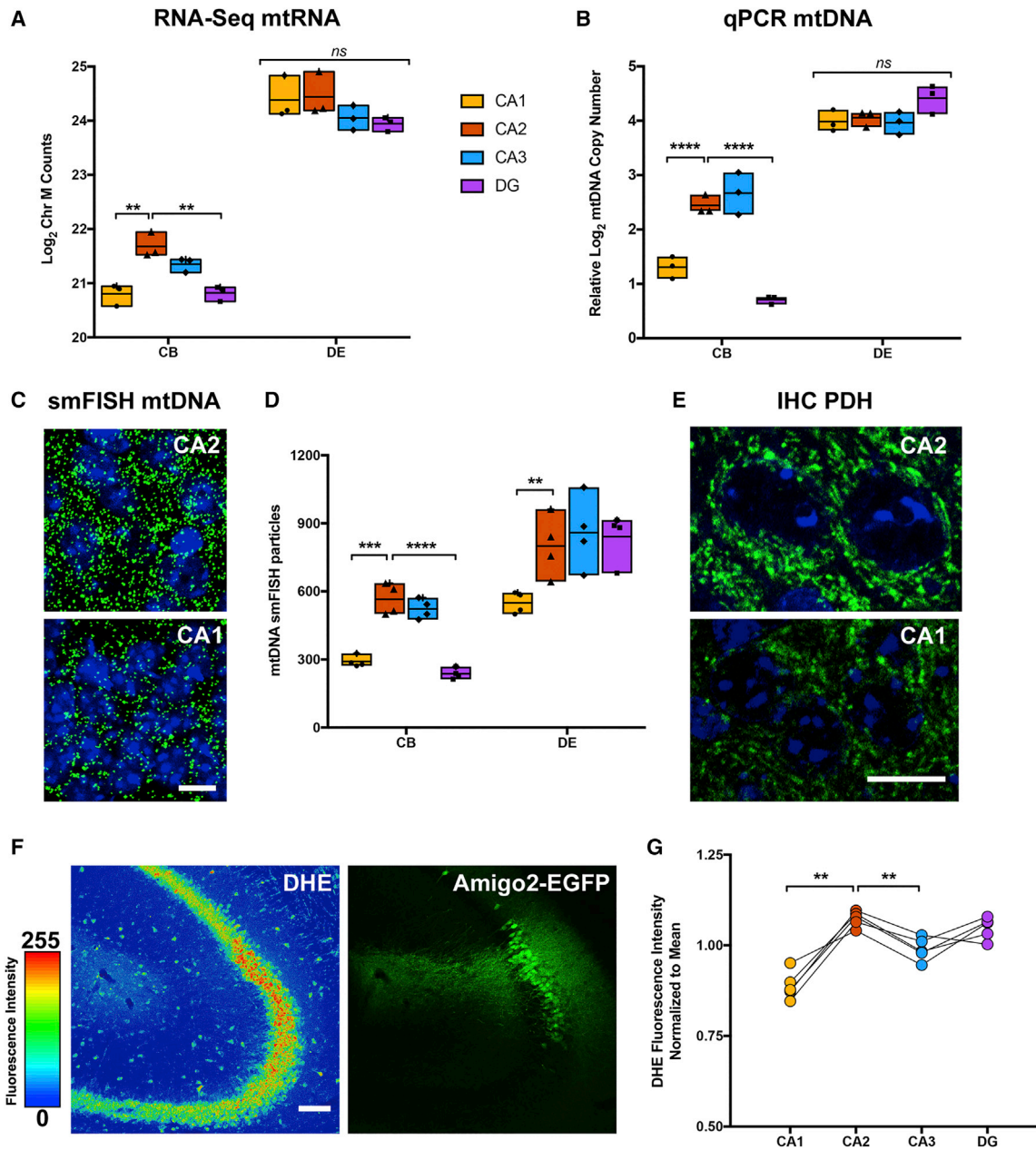


Figure 7. CA2 Neurons Have Greater Mitochondrial Content and Superoxide Production

(A) Transcription of mitochondrial genes on chromosome M (mtRNA) is highest in CA2 cell bodies with no differences detected in dendrites (compartment $p < 0.0001$, cell type $p = 0.0022$, interaction $p = 0.0297$; CB: CA2 versus CA1, $p = 0.0017$; CA2 versus CA3, $p = 0.2934$; CA2 versus DG, $p = 0.0020$; DE: CA2 versus CA1, $p = 0.9843$; CA2 versus CA3, $p = 0.1810$; CA2 versus DG, $p = 0.0703$; two-way ANOVA with Dunnett's post hoc tests; $N = 3$ mice).

(B) mtDNA copy number quantified using LCM-qPCR is highest in CA2 and CA3 cell bodies with no differences detected in dendrites (compartment $p < 0.0001$, cell type $p < 0.0001$, interaction $p < 0.0001$; CB: CA2 versus CA1, $p = 0.0001$; CA2 versus CA3, $p = 0.4828$; CA2 versus DG, $p = 0.0001$; DE: CA2 versus CA1, $p = 0.9583$; CA2 versus CA3, $p = 0.9229$; CA2 versus DG, $p = 0.1581$; two-way ANOVA with Dunnett's post hoc tests; $N = 3$ mice).

(C) smFISH images of mtDNA in CA2 and CA1 neurons.

(D) Quantification of smFISH particle counts for mtDNA copy number (compartment $p < 0.0001$, cell type $p < 0.0001$, interaction $p < 0.0015$; CB: CA2 versus CA1, $p = 0.0007$; CA2 versus CA3, $p = 0.8456$; CA2 versus DG, $p = 0.0001$; DE: CA2 versus CA1, $p = 0.0018$; CA2 versus CA3, $p = 0.6867$; CA2 versus DG, $p = 0.8604$; two-way ANOVA with Dunnett's post hoc tests; $N = 4$ mice).

(E) Confocal image of pyruvate dehydrogenase (PDH) staining in CA2 and CA1 neurons.

(F) Confocal image of an Amigo2-EGFP mouse injected with dihydroethidium (DHE; pseudocolored for intensity) to detect superoxide levels.

(legend continued on next page)

effect selectively at the CA2 synapses; however, the fact that continual protein synthesis in dendrites is required for maintaining synaptic responses in CA2 was further motivation for identifying which RNAs are present in CA2 dendrites.

Hippocampal Subregions Express Distinct Dendritic Transcriptomes

Previous studies have characterized cell-specific hippocampal transcriptomes at the single cell (Habib et al., 2016; Zeisel et al., 2015) and population (Cembrowski et al., 2016b) levels. These rich resources describe distinct transcriptomes for each major hippocampal subregion cell body but cannot address whether the corresponding dendrites have distinct transcriptomes, as they are lost when generating single-cell suspensions. In fact, prior to this work, no study had directly tested whether different excitatory cell types express distinct dendritic transcriptomes. High-throughput *in situ* hybridization studies (i.e., the Allen Brain Atlas; Lein et al., 2007) identified more than 50 cell-type-enriched dendritic RNAs (such as *Adcy1* in CA2), but the majority of dendritic RNAs are expressed in dendrites at levels well below the limit of detection for the chromogenic *in situ* methods that were used. Studies using microarray technology identified fewer than 200 RNAs in either adult rat CA1 dendrites (Zhong et al., 2006) or rat hippocampal neurites in culture (Poon et al., 2006), but these studies showed little overlap, suggesting that experimental conditions, such as age and/or days in culture and methods for isolating dendrites and neurites, may influence which RNAs are identified. The first study to use modern sequencing techniques on dendrites (Cajigas et al., 2012) identified more than 2500 RNAs in microdissected rat CA1 neuropil, a finding that fundamentally changed the way the field thinks about RNA localization. Since then, there has been more agreement on how many and which RNAs are dendritically localized, at least in CA1 (Ainsley et al., 2014; Cajigas et al., 2012; Nakayama et al., 2017). Another study looking at ribosome associated RNAs in cerebellar Purkinje cell (PC) dendrites saw some overlap with previously published CA1 dendritic RNAs but also identified PC-specific dendritic RNAs, suggesting that neurons in different brain regions might localize different subsets of RNAs (Kratz et al., 2014). However, our goal was to identify whether different cell types within the hippocampus that are known to express different forms of plasticity might also express distinct dendritic RNAs at the gene- and isoform-specific levels. We were particularly interested in the plasticity-resistant area CA2, which because of its poorly defined anatomical borders had yet to be precisely investigated. Indeed, we identified 1,055 cell-type-enriched dendritic RNAs, suggesting that depending on cell type, synaptic plasticity in the hippocampus may be differentially regulated at the level of local translation. This finding is consistent with our hypothesis, but we were still surprised at the large number of differentially expressed dendritic RNAs (~10% of all RNAs expressed in hippocampal neurons), which underscores the magnitude of RNA

regulation in dendrites and its potential impact on synaptic and behavioral plasticity. In agreement, we found that neuronal gene expression was over-represented in our high-confidence dendritic RNA list, but we cannot definitively rule out that some unvalidated hits may be due to differences in the composition of contaminating cell types. Dendritic RNAs require validation with smFISH to confirm dendritic expression. Nonetheless, this dataset raises the question of whether there are cell type-specific deficits in RNA localization that contribute to certain disease phenotypes. Moreover, recent work has shown that local translation also occurs in other classes of cells, such as astrocytes (Boulay et al., 2017; Sakers et al., 2017) and GABAergic neurons (Ouwenga et al., 2019) in addition to glutamatergic neurons both pre- and post-synaptically (Hafner et al., 2019), thus determining whether other classes of cells also express distinct localized transcriptomes, either within or across brain regions, will be of interest.

Cell-Type-Enriched Dendritic RNAs Have Longer UTRs and Are Abundantly Spliced

We were interested in identifying cell- and compartment-specific differences in isoform expression because it is well known that *cis*-regulatory elements and structures within RNA sequences (commonly in the 5' and 3' UTRs) together with *trans*-acting factors, such as RNA binding proteins (RBPs), dictate every step of RNA metabolism, from transcription to degradation (Moore, 2005). Many studies have shown that 3' UTRs are necessary and sufficient for dendritic localization, for example, *Camk2a* (Mori et al., 2000) and *Bdnf* (An et al., 2008; Andreassi and Riccio, 2009). Longer 3' UTRs provide larger platforms for RBPs and micro-RNAs (miRNAs) for greater regulatory control, and longer 3' UTRs have been described for activity-regulated (Chen et al., 2017; Dalal et al., 2017) and neurite-localized RNAs (Ouwenga et al., 2017; Tushev et al., 2018). Consistently, we also found that our high-confidence dendritic RNAs have longer 3' UTRs compared with both cell body-retained and non-pyramidal RNAs. Furthermore, our high-confidence dendritic RNAs that are protein coding are also more likely to contain a 3' UTR and slightly less likely to have rare or low-CAI codons compared with both cell body-retained and non-pyramidal RNAs. Moreover, in addition to the hundreds of cell type-specific alternative splicing differences we detected, we found that RNAs in each of our lists preferentially express distal over proximal 3' UTRs. Taken together, these data indicate that neuronal 3' UTRs often exhibit cell type-specific expression, are longer for localized transcripts and generally include distal exons.

Completely unexpected was that the majority of our splicing differences were from comparisons of dendrite samples across subregions. Further analyses pointed to a combination of potential explanations, including differential splicing from non-pyramidal cells within the dendritic lamina (such as *Ntrk2*) and subregion-specific dendritic splicing (such as *Shank2*), potentially involving local RNA processing (Andreassi et al., 2019;

(G) Quantification of the average DHE fluorescence in each subregion normalized to the mean per animal (overall effect of cell type $p = 0.0005$; CA2 versus CA1, $p = 0.0038$; CA2 versus CA3, $p = 0.0023$; CA2 versus DG, $p = 0.5723$; paired one-way ANOVA with Geisser-Greenhouse correction and Dunnett's post hoc tests; $N = 5$ mice).

Scale bars, 10 μm in (C) and (E), 100 μm in (F). * $p < 0.05$, ** $p < 0.01$, *** $p < 0.001$, and **** $p < 0.0001$. Data are presented as mean \pm SEM.

Tushev et al., 2018). Studies that have assessed alternative splicing in the hippocampus have typically done so with hippocampal lysates, which may have masked subregion- and/or cell-specific differences. This dataset will provide a wealth of information to future studies interesting in alternative splicing and RNA regulation in specific cell types of the hippocampus.

The Mitochondrial Calcium Uniporter Is Highest in CA2 and Regulates Synaptic Plasticity

Until recently, area CA2 has often been overlooked in the literature, likely because of its small size and poorly defined borders (Dudek et al., 2016). We therefore wanted to focus our analyses on area CA2 to try to identify classes of genes that might be involved in regulating unique CA2 properties, such as its resistance to plasticity, and after seeing the effects of protein synthesis inhibitors, baseline synaptic transmission. Unexpectedly, we found that RNAs implicated in mitochondrial pathways were overrepresented in CA2 cell bodies and dendrites compared with neighboring subregion cell bodies and dendrites. Specifically, we found both nuclear- and mitochondrially encoded RNAs were highest in CA2, the latter of which in cell bodies was due to the mtDNA's being present in CA2 at double the levels of neighboring CA1 and DG. We also identified a number of RNAs encoding proteins with known roles in mitochondrial calcium signaling, including those in the MCU complex, that were high in CA2 cell bodies and dendrites. Recently these data have been substantiated in a proteomic analysis of hippocampal tissue (Gerber et al., 2019).

Despite decades of study, the molecular identity of MCU was only recently identified by two groups in 2011 (Baughman et al., 2011; De Stefani et al., 2011). Since then, the molecules that make up and regulate the MCU complex are beginning to be identified (Kamer and Mootha, 2015). Interestingly, several but not all of the proteins thus far associated with MCU are enriched in CA2, including *Mcu*, *Micu1*, and *Mcur1*, but not others like *Micu2*, *Micu3*, and *Miro1* (also known as *Rhot1*) (Niescier et al., 2018), and some are even depleted from CA2, such as *Slc25a23* and *Mcub* (also known as *Ccdc109b* and known to have a dominant-negative effect on mitochondrial calcium uptake in HeLa cells (Raffaello et al., 2013)). Interestingly, loss of function mutations in *MCU1* leads to intellectual disability and myopathy in humans (Logan et al., 2014). A previous study evaluated the cell type-specific expression of the MCU complex in mouse and human hippocampus, but assessed only CA1 and CA3, and found similar expression differences in CA3 as we found in CA2 (Márkus et al., 2016). This is not surprising given that we found CA2 and CA3 cell body transcriptomes highly correlate with each other and have fewer differentially expressed genes when compared with each other versus compared with CA1 or DG (Table S3).

We also found that blocking mitochondrial calcium uptake altered the way plasticity is controlled at CA2 synapses. Specifically, blocking mitochondrial calcium uptake prior to giving an LTP pairing protocol, which would normally result in LTP in CA1 and no change in CA2, now induced long-term depression (LTD) in CA2 neurons. These data indicate that mitochondrial calcium uptake plays a critical role in regulating synaptic calcium levels, such that when mitochondrial calcium uptake is blocked,

synaptic calcium levels rise enough to allow LTD, but not to a level high enough to allow LTP. Thus, we propose that high mitochondrial calcium uptake is another plasticity limiting mechanism restricting LTP in CA2.

We also found that blocking mitochondrial calcium uptake produced cell type-specific effects on baseline synaptic responses. Namely, Ru360 enhanced baseline responses recorded from CA1 neurons while having little to no effect on those recorded from CA2 neurons. We speculate that differences in downstream calcium handling between CA1 and CA2 neurons contributed to the potentiation of responses in CA1 neurons but not in CA2 neurons. Indeed, a recent study showed that LTP induction at the CA3-CA1 Schafer collateral synapse is blunted when mitochondrial fission, a process that promotes mitochondrial calcium uptake, is blocked (Divakaruni et al., 2018). Thus, mitochondrial calcium uptake at synapses is regulated in a cell type-specific manner to differentially affect plasticity.

It remains an open question how mitochondria and local protein synthesis in dendrites are linked. A recent study found that locally fragmenting mitochondria in dendrites of neurons in culture resulted in fewer newly synthesized proteins and prevented the increase in spine head volume after a synaptic stimulation protocol (Rangaraju et al., 2019). Previous studies have shown in developing axons both *in vitro* and *in vivo* that mitochondria and RNA granules localize to axon branchpoints and that mitochondria provide ATP for translation of RNAs that promote actin-dependent branching (Spillane et al., 2013; Wong et al., 2017). Nuclear-encoded mitochondrial RNAs in axons have also been proposed to maintain mitochondrial function during neurite outgrowth (Gale et al., 2018; Cioni et al., 2019). Likely, then, local translation of mitochondrial RNAs will affect dendritic processes such as synaptic activity, but future studies testing how these processes interact are needed.

Mitochondrial Respiration Is Highest in CA2

Given that mitochondrial calcium levels positively regulate mitochondrial respiration (Llorente-Folch et al., 2015), we tested whether CA2 neurons produce more superoxide or reactive oxygen species (ROS) compared with neighboring subregions. We found that indeed CA2 neurons produced the most superoxide as indicated by higher levels of DHE staining, which is consistent with greater levels of mitochondrial respiration. Perplexingly, we detected the highest DHE staining in the CA2 cell body layer, and we failed to detect any differences across the dendritic laminae. We reason that DHE histology might not be sensitive enough to reveal differences, if any, in dendritic ROS production. One reason CA2 neurons may need greater levels of respiration is because of their higher average firing rate compared with neighboring hippocampal neurons in CA1 and CA3 (Alexander et al., 2016; Lu et al., 2015; Mankin et al., 2015). Notably, *Mcu* levels and the DHE staining both taper into CA3a, declining in intensity the more proximal they are to the DG. This is consistent with the mean firing rate gradient previously documented from CA2 to CA3 (Lu et al., 2015).

Moreover, with CA2 having the highest basal levels of ROS, one might conclude that CA2 neurons should be more vulnerable to neuronal insults, which are typically exacerbated

by mitochondrial dysfunction (Wang and Michaelis, 2010). However, it seems that the opposite is true, as CA2 neurons are resistant to neuronal injury in humans and animal models, such as with seizure and traumatic brain injury (Friedman et al., 2015; Kirino, 1982; Nadler et al., 1978; Sloviter et al., 1991; Yang et al., 2000). We speculate that this resistance might be due to a combination of factors intrinsic to CA2, such as the potential for higher glutathione activity (*Gsto1* is highest in CA2 neurons and dendrites) or greater calcium buffering and extrusion capacity (Simons et al., 2009) (of which mitochondria may play a role), both of which are known to contribute to the selective (in)vulnerability of neurons to oxidative stress. Further research is needed investigating how these processes work in concert to affect CA2 resistance to cell death, and we foresee this dataset being a fruitful resource for generating and informing future hypotheses implicating subregion-specific roles in disease pathophysiology.

STAR★METHODS

Detailed methods are provided in the online version of this paper and include the following:

- KEY RESOURCES TABLE
- LEAD CONTACT AND MATERIALS AVAILABILITY
- EXPERIMENTAL MODEL AND SUBJECT DETAILS
- METHOD DETAILS
 - Electrophysiology
 - Laser Capture Microdissection
 - Whole Transcriptome Microarray
 - RNaseq library construction
 - RNaseq analyses
 - Laser Capture Microdissection for gDNA qPCR
 - Quantification of mtDNA copy number using qPCR
 - Multiplexed single molecule fluorescent *in situ* hybridization
 - smFISH Image Acquisition and Quantification
 - Immunofluorescence
 - *In vivo* measurement of superoxide production
- QUANTIFICATION AND STATISTICAL ANALYSIS
- DATA AND CODE AVAILABILITY
- ADDITIONAL RESOURCES

SUPPLEMENTAL INFORMATION

Supplemental Information can be found online at <https://doi.org/10.1016/j.celrep.2019.08.093>.

ACKNOWLEDGMENTS

Research reported in this publication was supported by the National Institute of Mental Health of the NIH under award R00MH109626 (to S.F.) and by the Intramural Research Program of the NIH, National Institute of Environmental Health Sciences (Z01 ES100221 to S.M.D.). The content is solely the responsibility of the authors and does not necessarily represent the official views of the NIH. We thank Dr. Janine Santos and the members of the Dudek lab for feedback and critically reading this manuscript, as well as the NIEHS Epigenomics and DNA Sequencing Core Laboratory, Fluorescent Microscopy and Imaging Center, and animal care staff for their support.

AUTHOR CONTRIBUTIONS

Conceptualization, S.F. and S.M.D.; Methodology, S.F., J.M.W., Y.W., K.E.C., and M.S.; Software, S.F. and J.M.W.; Formal Analysis, S.F., J.M.W., K.E.C., and M.S.; Investigation, S.F., K.E.C., M.S., and Y.W.; Data Curation, J.M.W.; Writing – Original Draft, S.F.; Writing – Review & Editing, S.F., K.E.C., and S.M.D.; Visualization, S.F. and J.M.W.; Supervision, S.M.D.; Funding Acquisition, S.F. and S.M.D.

DECLARATION OF INTERESTS

The authors declare no conflict of interest or competing financial interest.

Received: June 28, 2018

Revised: August 15, 2019

Accepted: August 27, 2019

Published: October 8, 2019

SUPPORTING CITATIONS

The following reference appears in the Supplemental Information: Middleton et al. (2019).

REFERENCES

- Abraham, W.C., and Williams, J.M. (2008). LTP maintenance and its protein synthesis-dependence. *Neurobiol. Learn. Mem.* 89, 260–268.
- Ainsley, J.A., Drane, L., Jacobs, J., Kittelberger, K.A., and Reijmers, L.G. (2014). Functionally diverse dendritic mRNAs rapidly associate with ribosomes following a novel experience. *Nat. Commun.* 5, 4510.
- Alexander, G.M., Farris, S., Pirone, J.R., Zheng, C., Colgin, L.L., and Dudek, S.M. (2016). Social and novel contexts modify hippocampal CA2 representations of space. *Nat. Commun.* 7, 10300–10314.
- Alexander, G.M., Brown, L.Y., Farris, S., Lustberg, D., Pantazis, C., Gloss, B., Plummer, N.W., Jensen, P., and Dudek, S.M. (2018). CA2 neuronal activity controls hippocampal low gamma and ripple oscillations. *eLife* 7, e38052.
- An, J.J., Gharami, K., Liao, G.-Y., Woo, N.H., Lau, A.G., Vanevski, F., Torre, E.R., Jones, K.R., Feng, Y., Lu, B., et al. (2008). Distinct Role of Long 3' UTR BDNF mRNA in Spine Morphology and Synaptic Plasticity in Hippocampal Neurons. *Cell* 134, 175–187.
- Andreassi, C., and Riccio, A. (2009). To localize or not to localize: mRNA fate in 3' UTR ends. *Trends Cell Biol.* 19, 465–474.
- Andreassi, C., Luisier, R., Crerar, H., Blokzijl-Franke, S., Luscombe, N.M., Cuda, G., Gaspari, M., and Riccio, A. (2019). 3'UTR cleavage of transcripts localized in axons of sympathetic neurons. *bioRxiv*. <https://doi.org/10.1101/170100>.
- Andrews, S. (2010). FastQC: A quality control application for FastQ data. <http://www.bioinformatics.babraham.ac.uk/projects/fastqc/>.
- Aschrafi, A., Kar, A.N., Gale, J.R., Elkahoul, A.G., Vargas, J.N.S., Sales, N., Wilson, G., Tompkins, M., Gioio, A.E., and Kaplan, B.B. (2016). A heterogeneous population of nuclear-encoded mitochondrial mRNAs is present in the axons of primary sympathetic neurons. *Mitochondrion* 30, 18–23.
- Baughman, J.M., Perocchi, F., Girgis, H.S., Plovanich, M., Belcher-Timme, C.A., Sancak, Y., Bao, X.R., Strittmatter, L., Goldberger, O., Bogorad, R.L., et al. (2011). Integrative genomics identifies MCU as an essential component of the mitochondrial calcium uniporter. *Nature* 476, 341–345.
- Boulay, A.C., Saubaméa, B., Adam, N., Chasseigneaux, S., Mazaré, N., Gilbert, A., Bahin, M., Bastianelli, L., Blugeon, C., Perrin, S., et al. (2017). Translation in astrocyte distal processes sets molecular heterogeneity at the gliovascular interface. *Cell Discov.* 3, 17005.
- Burgin, K.E., Waxham, M.N., Rickling, S., Westgate, S.A., Mobley, W.C., and Kelly, P.T. (1990). *In situ* hybridization histochemistry of Ca²⁺/calmodulin-dependent protein kinase in developing rat brain. *J. Neurosci.* 10, 1788–1798.

- Cajigas, I.J., Tushev, G., Will, T.J., tom Dieck, S., Fuerst, N., and Schuman, E.M. (2012). The local transcriptome in the synaptic neuropil revealed by deep sequencing and high-resolution imaging. *Neuron* 74, 453–466.
- Carstens, K.E., Phillips, M.L., Pozzo-Miller, L., Weinberg, R.J., and Dudek, S.M. (2016). Perineuronal Nets Suppress Plasticity of Excitatory Synapses on CA2 Pyramidal Neurons. *J. Neurosci.* 36, 6312–6320.
- Carvalho, B.S., and Irizarry, R.A. (2010). A framework for oligonucleotide microarray preprocessing. *Bioinformatics* 26, 2363–2367.
- Cembrowski, M.S., Bachman, J.L., Wang, L., Sugino, K., Shields, B.C., and Spruston, N. (2016a). Spatial gene-expression gradients underlie prominent heterogeneity of CA1 pyramidal neurons. *Neuron* 89, 351–368.
- Cembrowski, M.S., Wang, L., Sugino, K., Shields, B.C., and Spruston, N. (2016b). Hipposeq: a comprehensive RNA-seq database of gene expression in hippocampal principal neurons. *eLife* 5, e14997.
- Chen, P.B., Kawaguchi, R., Blum, C., Achiro, J.M., Coppola, G., O'Dell, T.J., and Martin, K.C. (2017). Mapping gene expression in excitatory neurons during hippocampal late-phase long-term potentiation. *Front. Mol. Neurosci.* 10, 39.
- Cioni, J.-M., Lin, J.Q., Holtermann, A.V., Koppers, M., Jakobs, M.A.H., Azizi, A., Turner-Bridger, B., Shigeoka, T., Franze, K., Harris, W.A., and Holt, C.E. (2019). Late endosomes act as mRNA translation platforms and sustain mitochondria in axons. *Cell* 176, 56–72.e15.
- ENCODE Project Consortium (2012). An integrated encyclopedia of DNA elements in the human genome. *Nature* 488, 57–74.
- Culhane, A.C., Perrière, G., Conside, E.C., Cotter, T.G., and Higgins, D.G. (2002). Between-group analysis of microarray data. *Bioinformatics* 18, 1600–1608.
- Dalal, J.S., Yang, C., Sapkota, D., Lake, A.M., O'Brien, D.R., and Dougherty, J.D. (2017). Quantitative nucleotide level analysis of regulation of translation in response to depolarization of cultured neural cells. *Front. Mol. Neurosci.* 10, 9.
- De Stefani, D., Raffaello, A., Teardo, E., Szabò, I., and Rizzuto, R. (2011). A forty-kilodalton protein of the inner membrane is the mitochondrial calcium uniporter. *Nature* 476, 336–340.
- Devaraju, P., Yu, J., Eddins, D., Mellado-Lagarde, M.M., Earls, L.R., Westmoreland, J.J., Quarato, G., Green, D.R., and Zakharenko, S.S. (2017). Haploinsufficiency of the 22q11.2 microdeletion gene MRP140 disrupts short-term synaptic plasticity and working memory through dysregulation of mitochondrial calcium. *Mol. Psychiatry* 22, 1313–1326.
- Divakaruni, S.S., Van Dyke, A.M., Chandra, R., LeGates, T.A., Contreras, M., Dharmasri, P.A., Higgs, H.N., Lobo, M.K., Thompson, S.M., and Blanpied, T.A. (2018). Long-term potentiation requires a rapid burst of dendritic mitochondrial fission during induction. *Neuron* 100, 860–875.e7.
- Dobin, A., Davis, C.A., Schlesinger, F., Drenkow, J., Zaleski, C., Jha, S., Batut, P., Chaisson, M., and Gingeras, T.R. (2013). STAR: ultrafast universal RNA-seq aligner. *Bioinformatics* 29, 15–21.
- Donlin-Asp, P.G., Rossoll, W., and Bassell, G.J. (2017). Spatially and temporally regulating translation via mRNA-binding proteins in cellular and neuronal function. *FEBS Lett.* 591, 1508–1525.
- Dudek, S.M., Alexander, G.M., and Farris, S. (2016). Rediscovering area CA2: unique properties and functions. *Nat. Rev. Neurosci.* 17, 89–102.
- Epstein, I., Tushev, G., Will, T.J., Vlatkovic, I., Cajigas, I.J., and Schuman, E.M. (2013). Alternative polyadenylation and differential expression of Shank mRNAs in the synaptic neuropil. *Philos. Trans. R. Soc. Lond. B Biol. Sci.* 369, 20130137.
- Farris, S., Wang, Y., Ward, J.M., and Dudek, S.M. (2017). Optimized method for robust transcriptome profiling of minute tissues using laser capture microdissection and low-input RNA-seq. *Front. Mol. Neurosci.* 10, 185.
- Floyd, B.J., Wilkerson, E.M., Veling, M.T., Minogue, C.E., Xia, C., Beebe, E.T., Wrobel, R.L., Cho, H., Kremer, L.S., Alston, C.L., et al. (2016). Mitochondrial protein interaction mapping identifies regulators of respiratory chain function. *Mol. Cell* 63, 621–632.
- Friedman, L.K., Slomko, A.M., Wongvavrit, J.P., Naseer, Z., Hu, S., Wan, W.Y., and Ali, S.S. (2015). Efficacy of retigabine on acute limbic seizures in adult rats. *J. Epilepsy Res.* 5, 46–59.
- Furda, A., Santos, J.H., Meyer, J.N., and Van Houten, B. (2014). Quantitative PCR-based measurement of nuclear and mitochondrial DNA damage and repair in mammalian cells. *Methods Mol. Biol.* 1105, 419–437.
- Gale, J.R., Aschrafi, A., Gioio, A.E., and Kaplan, B.B. (2018). Nuclear-encoded mitochondrial mRNAs: a powerful force in axonal growth and development. *Neuroscientist* 24, 142–155.
- Gerber, K.J., Dammer, E.B., Duong, D.M., Deng, Q., Dudek, S.M., Seyfried, N.T., and Hepler, J.R. (2019). Specific proteomes of hippocampal regions CA2 and CA1 reveal proteins linked to the unique physiology of area CA2. *J. Proteome Res.* 18, 2571–2584.
- Grooms, S.Y., Noh, K.M., Regis, R., Bassell, G.J., Bryan, M.K., Carroll, R.C., and Zukin, R.S. (2006). Activity bidirectionally regulates AMPA receptor mRNA abundance in dendrites of hippocampal neurons. *J. Neurosci.* 26, 8339–8351.
- Habib, N., Li, Y., Heidenreich, M., Swiech, L., Avraham-Davidi, I., Trombetta, J.J., Hession, C., Zhang, F., and Regev, A. (2016). Div-Seq: single-nucleus RNA-seq reveals dynamics of rare adult newborn neurons. *Science* 353, 925–928.
- Hafner, A.-S., Donlin-Asp, P.G., Leitch, B., Herzog, E., and Schuman, E.M. (2019). Local protein synthesis is a ubiquitous feature of neuronal pre- and postsynaptic compartments. *Science* 364, eaau3644.
- Hagena, H., and Manahan-Vaughan, D. (2013). Differentiation in the protein synthesis-dependency of persistent synaptic plasticity in mossy fiber and associational/commissural CA3 synapses in vivo. *Front. Integr. Neurosci.* 7, 10.
- Hitti, F.L., and Siegelbaum, S.A. (2014). The hippocampal CA2 region is essential for social memory. *Nature* 508, 88–92.
- Holt, C.E., and Schuman, E.M. (2013). The central dogma decentralized: new perspectives on RNA function and local translation in neurons. *Neuron* 80, 648–657.
- Hu, D., Serrano, F., Oury, T.D., and Klann, E. (2006). Aging-dependent alterations in synaptic plasticity and memory in mice that overexpress extracellular superoxide dismutase. *J. Neurosci.* 26, 3933–3941.
- Joshi, N.A., and Fass, J.N. (2011). Sickle: a sliding-window, adaptive, quality-based trimming tool for FastQ files (Version 1.33). <https://github.com/najoshi/sickle.git>.
- Ju, W., Morishita, W., Tsui, J., Gaietta, G., Deerinck, T.J., Adams, S.R., Garner, C.C., Tsien, R.Y., Ellisman, M.H., and Malenka, R.C. (2004). Activity-dependent regulation of dendritic synthesis and trafficking of AMPA receptors. *Nat. Neurosci.* 7, 244–253.
- Kamer, K.J., and Mootha, V.K. (2015). The molecular era of the mitochondrial calcium uniporter. *Nat. Rev. Mol. Cell Biol.* 16, 545–553.
- Kandel, E.R., Dudai, Y., and Mayford, M.R. (2014). The molecular and systems biology of memory. *Cell* 157, 163–186.
- Kiebler, M.A., Scheiffele, P., and Ule, J. (2013). What, where, and when: the importance of post-transcriptional regulation in the brain. *Front. Neurosci.* 7, 192.
- Kirino, T. (1982). Delayed neuronal death in the gerbil hippocampus following ischemia. *Brain Res.* 239, 57–69.
- Kratz, A., Beguin, P., Kaneko, M., Chimura, T., Suzuki, A.M., Matsunaga, A., Kato, S., Bertin, N., Lassmann, T., Vigot, R., et al. (2014). Digital expression profiling of the compartmentalized transcriptome of Purkinje neurons. *Genome Res.* 24, 1396–1410.
- Kupersmidt, I., Su, Q.J., Grewal, A., Sundaresh, S., Halperin, I., Flynn, J., Shekar, M., Wang, H., Park, J., Cui, W., et al. (2010). Ontology-based meta-analysis of global collections of high-throughput public data. *PLoS ONE* 5, e13066.
- Lee, S.E., Simons, S.B., Heldt, S.A., Zhao, M., Schroeder, J.P., Vellano, C.P., Cowan, D.P., Ramineni, S., Yates, C.K., Feng, Y., et al. (2010). RGS14 is a natural suppressor of both synaptic plasticity in CA2 neurons and hippocampal-based learning and memory. *Proc. Natl. Acad. Sci. U S A* 107, 16994–16998.

- Lein, E.S., Hawrylycz, M.J., Ao, N., Ayres, M., Bensinger, A., Bernard, A., Boe, A.F., Boguski, M.S., Brockway, K.S., Byrnes, E.J., et al. (2007). Genome-wide atlas of gene expression in the adult mouse brain. *Nature* **445**, 168–176.
- Leroy, F., Brann, D.H., Meira, T., and Siegelbaum, S.A. (2017). Input-timing-dependent plasticity in the hippocampal CA2 region and its potential role in social memory. *Neuron* **95**, 1089–1102.e5.
- Liao, Y., Smyth, G.K., and Shi, W. (2014). featureCounts: an efficient general purpose program for assigning sequence reads to genomic features. *Bioinformatics* **30**, 923–930.
- Lin, Y.-T., Hsieh, T.-Y., Tsai, T.-C., Chen, C.-C., Huang, C.-C., and Hsu, K.-S. (2018). Conditional deletion of hippocampal CA2/CA3a oxytocin receptors impairs the persistence of long-term social recognition memory in mice. *J. Neurosci.* **38**, 1218–1231.
- Llorente-Folch, I., Rueda, C.B., Pardo, B., Szabadkai, G., Duchon, M.R., and Satrustegui, J. (2015). The regulation of neuronal mitochondrial metabolism by calcium. *J. Physiol.* **593**, 3447–3462.
- Logan, C.V., Szabadkai, G., Sharpe, J.A., Parry, D.A., Torelli, S., Childs, A.-M., Kriek, M., Phadke, R., Johnson, C.A., Roberts, N.Y., et al.; UK10K Consortium (2014). Loss-of-function mutations in MICU1 cause a brain and muscle disorder linked to primary alterations in mitochondrial calcium signaling. *Nat. Genet.* **46**, 188–193.
- Love, M.I., Huber, W., and Anders, S. (2014). Moderated estimation of fold change and dispersion for RNA-seq data with DESeq2. *Genome Biol.* **15**, 550.
- Lu, L., Igarashi, K.M., Witter, M.P., Moser, E.I., and Moser, M.-B. (2015). Topography of place maps along the CA3-to-CA2 axis of the hippocampus. *Neuron* **87**, 1078–1092.
- Mankin, E.A., Diehl, G.W., Sparks, F.T., Leutgeb, S., and Leutgeb, J.K. (2015). Hippocampal CA2 activity patterns change over time to a larger extent than between spatial contexts. *Neuron* **85**, 190–201.
- Márkus, N.M., Hasel, P., Qiu, J., Bell, K.F.S., Heron, S., Kind, P.C., Dando, O., Simpson, T.I., and Hardingham, G.E. (2016). Expression of mRNA encoding Mcu and other mitochondrial calcium regulatory genes depends on cell type, neuronal subtype, and Ca²⁺ signaling. *PLoS ONE* **11**, e0148164–e16.
- Martin, M. (2011). Cutadapt removes adapter sequences from high-throughput sequencing reads. *EMBnet journal* **17**, 10–12.
- McCormack, J.G., Halestrap, A.P., and Denton, R.M. (1990). Role of calcium ions in regulation of mammalian intramitochondrial metabolism. *Physiol. Rev.* **70**, 391–425.
- Meira, T., Leroy, F., Buss, E.W., Oliva, A., Park, J., and Siegelbaum, S.A. (2018). A hippocampal circuit linking dorsal CA2 to ventral CA1 critical for social memory dynamics. *Nat. Commun.* **9**, 4163.
- Middlemas, D.S., Lindberg, R.A., and Hunter, T. (1991). trkB, a neural receptor protein-tyrosine kinase: evidence for a full-length and two truncated receptors. *Mol. Cell. Biol.* **11**, 143–153.
- Middleton, S.A., Eberwine, J., and Kim, J. (2019). Comprehensive catalog of dendritically localized mRNA isoforms from sub-cellular sequencing of single mouse neurons. *BMC Biol.* **17**, 5.
- Moore, M.J. (2005). From birth to death: the complex lives of eukaryotic mRNAs. *Science* **309**, 1514–1518.
- Mori, Y., Imaizumi, K., Katayama, T., Yoneda, T., and Tohyama, M. (2000). Two cis-acting elements in the 3' untranslated region of α -CaMKII regulate its dendritic targeting. *Nat. Neurosci.* **3**, 1079–1084.
- Nadler, J.V., Perry, B.W., and Cotman, C.W. (1978). Intraventricular kainic acid preferentially destroys hippocampal pyramidal cells. *Nature* **271**, 676–677.
- Nakamura, Y., Gojobori, T., and Ikemura, T. (2000). Codon usage tabulated from international DNA sequence databases: status for the year 2000. *Nucleic Acids Res.* **28**, 292.
- Nakayama, K., Ohashi, R., Shinoda, Y., Yamazaki, M., Abe, M., Fujikawa, A., Shigenobu, S., Futatsugi, A., Noda, M., Mikoshiba, K., et al. (2017). RNG105/caprin1, an RNA granule protein for dendritic mRNA localization, is essential for long-term memory formation. *eLife* **6**, e29677.
- Niescier, R.F., Hong, K., Park, D., and Min, K.-T. (2018). MCU Interacts with Miro1 to Modulate Mitochondrial Functions in Neurons. *J. Neurosci.* **38**, 4666–4677.
- Ouwenga, R., Lake, A.M., O'Brien, D., Mogha, A., Dani, A., and Dougherty, J.D. (2017). Transcriptomic analysis of ribosome-bound mRNA in cortical neurites *in vivo*. *J. Neurosci.* **37**, 8688–8705.
- Ouwenga, R., Lake, A.M., Aryal, S., Lagunas, T., and Dougherty, J.D. (2019). The differences in local translation across distinct neuron types is mediated by both baseline cellular differences and post-transcriptional mechanisms. *ENeuro* **4**, ENEURO.0320-18.2018.
- Pagani, J.H., Zhao, M., Cui, Z., Avram, S.K., Caruana, D.A., Dudek, S.M., and Young, W.S. (2015). Role of the vasopressin 1b receptor in rodent aggressive behavior and synaptic plasticity in hippocampal area CA2. *Mol. Psychiatry* **20**, 490–499.
- Paillard, M., Csordás, G., Szanda, G., Golenár, T., Debattisti, V., Bartok, A., Wang, N., Moffat, C., Seifert, E.L., Spät, A., and Hajnóczky, G. (2017). Tissue-specific mitochondrial decoding of cytoplasmic Ca²⁺ signals is controlled by the stoichiometry of MICU1/2 and MCU. *Cell Rep.* **18**, 2291–2300.
- Patro, R., Duggal, G., Love, M.I., Irizarry, R.A., and Kingsford, C. (2017). Salmon provides fast and bias-aware quantification of transcript expression. *Nat. Methods* **14**, 417–419.
- Poon, M.M., Choi, S.H., Jamieson, C.A.M., Geschwind, D.H., and Martin, K.C. (2006). Identification of process-localized mRNAs from cultured rodent hippocampal neurons. *J. Neurosci.* **26**, 13390–13399.
- Raam, T., McAvoy, K.M., Besnard, A., Veenema, A.H., and Sahay, A. (2017). Hippocampal oxytocin receptors are necessary for discrimination of social stimuli. *Nat. Commun.* **8**, 2001.
- Raffaello, A., De Stefani, D., Sabbadin, D., Teardo, E., Merli, G., Picard, A., Checchetto, V., Moro, S., Szabó, I., and Rizzuto, R. (2013). The mitochondrial calcium uniporter is a multimer that can include a dominant-negative pore-forming subunit. *EMBO J.* **32**, 2362–2376.
- Rangaraju, V., Lauterbach, M., and Schuman, E.M. (2019). Spatially stable mitochondrial compartments fuel local translation during plasticity. *Cell* **176**, 73–84.e15.
- Rose, C.R., Blum, R., Pichler, B., Lepier, A., Kafitz, K.W., and Konnerth, A. (2003). Truncated TrkB-T1 mediates neurotrophin-evoked calcium signalling in glia cells. *Nature* **426**, 74–78.
- Sakers, K., Lake, A.M., Khazanchi, R., Ouwenga, R., Vasek, M.J., Dani, A., and Dougherty, J.D. (2017). Astrocytes locally translate transcripts in their peripheral processes. *Proc. Natl. Acad. Sci. U S A* **114**, E3830–E3838.
- Schindelin, J., Arganda-Carreras, I., Frise, E., Kaynig, V., Longair, M., Pietzsch, T., Preibisch, S., Rueden, C., Saalfeld, S., Schmid, B., et al. (2012). Fiji: an open-source platform for biological-image analysis. *Nat. Methods* **9**, 676–682.
- Sharp, P.M., and Li, W.H. (1987). The codon adaptation index—a measure of directional synonymous codon usage bias, and its potential applications. *Nucleic Acids Res.* **15**, 1281–1295.
- Shigeoka, T., Jung, H., Jung, J., Turner-Bridger, B., Ohk, J., Lin, J.Q., Amieux, P.S., and Holt, C.E. (2016). Dynamic axonal translation in developing and mature visual circuits. *Cell* **166**, 181–192.
- Simons, S.B., Escobedo, Y., Yasuda, R., and Dudek, S.M. (2009). Regional differences in hippocampal calcium handling provide a cellular mechanism for limiting plasticity. *Proc. Natl. Acad. Sci. U S A* **106**, 14080–14084.
- Sims, D., Sudbery, I., Ilott, N.E., Heger, A., and Ponting, C.P. (2014). Sequencing depth and coverage: key considerations in genomic analyses. *Nat. Rev. Genet.* **15**, 121–132.
- Sloviter, R.S., Sollas, A.L., Barbaro, N.M., and Laxer, K.D. (1991). Calcium-binding protein (calbindin-D28K) and parvalbumin immunocytochemistry in the normal and epileptic human hippocampus. *J. Comp. Neurol.* **308**, 381–396.
- Smith, A.S., Williams Avram, S.K., Cymerblit-Sabba, A., Song, J., and Young, W.S. (2016). Targeted activation of the hippocampal CA2 area strongly enhances social memory. *Mol. Psychiatry* **21**, 1137–1144.

- Smyth, G.K. (2005). limma: linear models for microarray data. In *Bioinformatics and Computational Biology Solutions Using R and Bioconductor*, R. Gentleman, V.J. Carey, W. Huber, R.A. Irizarry, and S. Dudoit, eds. (Springer-Verlag), pp. 397–420.
- Sommer, B., Keinänen, K., Verdoorn, T.A., Wisden, W., Burnashev, N., Herb, A., Köhler, M., Takagi, T., Sakmann, B., and Seeburg, P.H. (1990). Flip and flop: a cell-specific functional switch in glutamate-operated channels of the CNS. *Science* 249, 1580–1585.
- Spillane, M., Ketschek, A., Merianda, T.T., Twiss, J.L., and Gallo, G. (2013). Mitochondria coordinate sites of axon branching through localized intraxonal protein synthesis. *Cell Rep.* 5, 1564–1575.
- Steward, O., and Schuman, E.M. (2001). Protein synthesis at synaptic sites on dendrites. *Annu. Rev. Neurosci.* 24, 299–325.
- Taliaferro, J.M., Vidaki, M., Oliveira, R., Olson, S., Zhan, L., Saxena, T., Wang, E.T., Graveley, B.R., Gertler, F.B., Swanson, M.S., and Burge, C.B. (2016). Distal alternative last exons localize mRNAs to neural projections. *Mol. Cell* 61, 821–833.
- Tollefson, K.E., Kroczyński, J., and Cutaia, M.V. (2003). Time-dependent interactions of oxidant-sensitive fluoroprobes with inhibitors of cellular metabolism. *Lab. Invest.* 83, 367–375.
- Tushev, G., Glock, C., Heumüller, M., Biever, A., Jovanovic, M., and Schuman, E.M. (2018). Alternative 3' UTRs modify the localization, regulatory potential, stability, and plasticity of mRNAs in neuronal compartments. *Neuron* 98, 495–511.e6.
- Wang, X., and Michaelis, E.K. (2010). Selective neuronal vulnerability to oxidative stress in the brain. *Front. Aging Neurosci.* 2, 12.
- Watson, C., and Paxinos, G. (2010). *Chemoarchitectonic Atlas of the Mouse Brain* (Academic Press).
- Wong, H.H.-W., Lin, J.Q., Ströhl, F., Roque, C.G., Cioni, J.-M., Cagnetta, R., Turner-Bridger, B., Laine, R.F., Harris, W.A., Kaminski, C.F., and Holt, C.E. (2017). RNA docking and local translation regulate site-specific axon remodeling in vivo. *Neuron* 95, 852–868.e8.
- Yang, G., Kitagawa, K., Ohtsuki, T., Kuwabara, K., Mabuchi, T., Yagita, Y., Takazawa, K., Tanaka, S., Yanagihara, T., Hori, M., and Matsumoto, M. (2000). Regional difference of neuronal vulnerability in the murine hippocampus after transient forebrain ischemia. *Brain Res.* 870, 195–198.
- Yoon, B.C., Jung, H., Dwivedy, A., O'Hare, C.M., Zivraj, K.H., and Holt, C.E. (2012). Local translation of extranuclear lamin B promotes axon maintenance. *Cell* 148, 752–764.
- Zeisel, A., Muñoz-Manchado, A.B., Codeluppi, S., Lönnerberg, P., La Manno, G., Juréus, A., Marques, S., Munguba, H., He, L., Betsholtz, C., et al. (2015). Brain structure. Cell types in the mouse cortex and hippocampus revealed by single-cell RNA-seq. *Science* 347, 1138–1142.
- Zhang, Y., Chen, K., Sloan, S.A., Bennett, M.L., Scholze, A.R., O'Keefe, S., Phatnani, H.P., Guarnieri, P., Caneda, C., Ruderisch, N., et al. (2014). An RNA-sequencing transcriptome and splicing database of glia, neurons, and vascular cells of the cerebral cortex. *J. Neurosci.* 34, 11929–11947.
- Zhao, M., Choi, Y.S., Obrietan, K., and Dudek, S.M. (2007). Synaptic plasticity (and the lack thereof) in hippocampal CA2 neurons. *J. Neurosci.* 27, 12025–12032.
- Zhou, Z., and Bers, D.M. (2002). Time course of action of antagonists of mitochondrial Ca uptake in intact ventricular myocytes. *Pflügers Arch.* 445, 132–138.
- Zhong, J., Zhang, T., and Bloch, L.M. (2006). Dendritic mRNAs encode diversified functionalities in hippocampal pyramidal neurons. *BMC Neurosci.* 7, 17.

STAR★METHODS

KEY RESOURCES TABLE

REAGENT or RESOURCE	SOURCE	IDENTIFIER
Antibodies		
mouse anti-RGS14	UC Davis/NIH NeuroMab Facility	Cat# AB_2179931; RRID:AB_10698026
mouse anti-STEP	Cell Signaling	Cat# 4817; RRID:AB_2173544;
rabbit anti-PCP4	Santa Cruz Biotechnology	Cat# sc-74186
mouse anti- pyruvate dehydrogenase E1	Cell Signaling	Cat# AB110333; RRID:AB_10862029
rabbit anti-EFCBP2 (NECAB2)	Novus Biologicals	Cat# NBP1-84002; RRID:AB_11028373
rabbit anti-COXIV	Synaptic Systems	Cat# 298 003; RRID:AB_2620042
Chemicals, Peptides, and Recombinant Proteins		
Ru360	Millipore Sigma	Cat #557440
dihydroethidium	ThermoFisherScientific	Cat# D1168
Critical Commercial Assays		
Ovation Universal RNA-seq system for mouse	Nugen	Cat# 0348
RNAscope Fluorescent Multiplex kit instructions	Advanced Cell Diagnostics	Cat# 320850
PicoPure RNA Isolation kit	Arcturus	Cat# KIT0202
Deposited Data		
RNA-seq and Microarray data	Gene Expression Omnibus	GEO: GSE116343
single cell RNA-seq data from mouse cortex	http://www.brainrnaseq.org/	N/A
Experimental Models: Organisms/Strains		
Amigo2-EGFP transgenic mice	GENSAT founder line LW244	RRID: MMRRC_033018-UCD
Software and Algorithms		
Salmon	Patro et al., 2017	v0.9.1
STAR	Dobin et al., 2013	v2.5.1b
limma	Smyth, 2005	v3.32.2
featureCounts	Liao et al., 2014	v1.5.1
DESeq2	Love et al., 2014	v1.18.1
Fiji	Schindelin et al., 2012	v2
Jampack	This paper; https://github.com/jmw86069/jampack	N/A
Splicejam	This paper; http://splicejam.vtc.vt.edu/ ; https://jmw86069.github.io/splicejam/index.html ;	N/A

LEAD CONTACT AND MATERIALS AVAILABILITY

Further information and requests for resources and reagents should be directed to and will be fulfilled by the Lead Contact, Serena Dudek (dudek@niehs.nih.gov). This study did not generate new unique reagents.

EXPERIMENTAL MODEL AND SUBJECT DETAILS

For all experiments, except electrophysiology experiments, adult male and female Amigo2-EGFP transgenic mice (GENSAT founder line LW244 RRID: [MMRRC_033018-UCD](https://www.ncbi.nlm.nih.gov/rrids/RRID:MMRRC_033018-UCD)) that had been bred for at least 10 generations onto C57BL/6J background were used. For electrophysiology experiments, C57BL/6J pregnant dams were purchased from Charles River Laboratories. Mice were group housed under a 12:12 light/dark cycle with access to food and water *ad libitum*. All procedures were approved by the Animal Care and Use Committee of NIEHS and were in accordance with the National Institutes of Health guidelines for care and use of animals.

METHOD DETAILS

Electrophysiology

Translation inhibitor study

Mice age P13-17 of either sex mice were deeply anaesthetized with pentobarbital (tradename: FatalPlus). Brains were then rapidly removed and placed in an ice-cold sucrose cutting solution containing the following (in mM): 240 sucrose, 2.0 KCl, 1 MgCl₂, 2 MgSO₄, 1 CaCl₂, 1.25 NaH₂PO₄, 26 NaHCO₃ and 10 glucose. Parasagittal hippocampal slices (300 μm) were obtained using a vibrating microtome (Leica VT 1000S). As slices were collected, they were placed into a holding chamber with ACSF containing the following (in mM) 124 NaCl, 2.5 KCl, 2 MgCl₂, 2 CaCl₂, 1.25 NaH₂PO₄, 26 NaHCO₃, and 17 d-glucose bubbled with 95% O₂ with 5% CO₂. To recover, slices were kept in a water bath held at approximately 35° for 30 minutes before being kept at room temperature for the remainder of the recovery period (minimum 30 minutes).

In vitro whole cell patch clamp recordings were performed on CA2 or CA1 pyramidal cells. During recordings, parasagittal hippocampal slices were placed in a submerged chamber and continuously perfused with ACSF (room temperature) at a flow rate of 2ml/minute. All patch clamp recordings were made in voltage clamp mode held at –70mV using patch pipettes fabricated from borosilicate glass capillaries and pulled using a horizontal puller (P97, Sutter Instrument), with a resistance of 2-5MΩ. Glass borosilicate pipettes were filled with a cesium based intracellular solution containing (in mM): 115 Cs-methanesulfonate, 20 CsCl, 2.5 MgCl₂, 0.6 EGTA, 10 HEPES, 4 Na₂-ATP, 0.4 Na-GTP, and 10 phosphocreatine disodium salt, pH 7.2, osmolarity 280-300 mOsm. Postsynaptic responses (PSCs) were evoked every 30 s with a 0.1ms pulse using a 2-contact cluster electrode (FHC, USA), placed in the stratum radiatum to target Schaffer collateral inputs from CA3. Data was acquired using an Axopatch 200B amplifier (Molecular Devices) and WinLTP software, filtered at 2kHz and digitised at a sampling rate of 20kHz using Digidata 1322A (Molecular Devices). The amplitude of PSC responses was measured using a 5-20ms after pulse detection period. Series and input resistance was monitored using a –4mV hyperpolarizing step. Data from experiments with a > 20% change in series resistance were discarded.

Following a 10-minute period of stable baseline responses, cycloheximide (60 μM in ACSF), anisomycin (20 μM in 0.1% DMSO) or vehicle was applied for the remaining duration of the experiment. For plotting and analyzing data, 2 consecutive sweeps (taken every 30 s) were averaged using WinLTP reanalysis software to acquire measurements every minute. PSC amplitude was normalized to baseline and SigmaPlot was used for graphical representation. For statistical analysis, t tests were carried out using SPSS software to compare raw PSC amplitude before and after drug or vehicle application. To compare PSC amplitude following cycloheximide and anisomycin application with their respective vehicle controls, normalized PSC amplitude was compared during the last 10 minutes of application.

MCU inhibitor study

Mice age P13-18 of either sex mice were deeply anaesthetized with pentobarbital (tradename: FatalPlus). We verified by smFISH that *Mcu* expression is enriched in CA2 by at least P14 (N = 3 mice, data not shown). Coronal brain slices were cut at 300 μm using a vibrating microtome (Leica VT 1000S). Drug Ru360 10 μM (Millipore Sigma, Cat #557440, [Devaraju et al., 2017](#); [Zhou and Bers, 2002](#)) was added to the patch pipet solution and concealed from light. Glass borosilicate pipettes were filled with a potassium gluconate internal solution (in mM) 120 K-gluconate, 10 KCl, 3 MgCl₂, 0.5 EGTA, 40 HEPES, 2 Na₂-ATP, 0.3 Na-GTP, pH 7.2). For LTP experiments, a pairing protocol was used; 1.5 minutes of 3 Hz presynaptic stimulation (270 pulses) paired with postsynaptic depolarization to 0 mV in voltage-clamp mode. Data were collected using Clampex 10.4 and analyzed using Clampfit software (Axon Instruments). Series and input resistances were monitored by measuring the response to a 10 mV step at each sweep and cells were included for analysis if < 25% change in series and input resistance.

Laser Capture Microdissection

To precisely delineate the CA2 borders, we used the transgenic mouse line (Amigo2-EGFP) that selectively expresses enhanced green fluorescent protein (EGFP) in CA2 cell bodies and dendrites ([Figure 1](#)). Neighboring subregions were identified using anatomical borders in bright field. Cognizant of the transcriptional heterogeneity in the hippocampus, in particular along the dorsal-ventral axis ([Cembrowski et al., 2016a](#)), we focused on the dorsal hippocampus, which is easily distinguishable from ventral hippocampus in the sagittal plane. For individual subregions, we focused on the suprapyramidal blade of the dentate gyrus, distal CA3 (closest to CA2), all of CA2, and the majority of CA1 midway along the proximal-distal axis including both superficial and deep layers (see [Figure 2A](#)). Three 6-8-week-old male mice from separate litters were used for the main study. Tissue was harvested within a 2-hour time window near the end of the light cycle (3-5pm, lights off 6pm). Mice were deeply anesthetized with Fatal Plus (50mg/kg) before swift removal of the brain (< 2 min). Brains were bisected in the sagittal plane and individually flash frozen by being placed in a 22 × 22mm disposable cryomold (Polysciences, Inc.) filled with Optimal Cutting Temperature compound and submerged in isopentane cooled to –20C on a dry ice and ethanol slurry. Samples were stored at –80C until LCM.

From each subfield (CA1, CA2, CA3 & DG), approximately 100 eight-micron thick cryosections were collected from the cell body and apical dendritic regions using a Pixcell II LCM instrument (Arcturus) equipped with a fluorescence microscope and infrared (IR) laser as described in detail in Farris et al., 2017 ([Farris et al., 2017](#)). The number of biological replicates and use of one sex was constrained by the cost of sequencing at the coverage depth required for alternative splice variant detection ([Sims et al., 2014](#)). Prior to LCM, a few sections were stained with cresyl violet to verify coordinates (Dorsal Hippocampus: 1.00mm to 2.00mm lateral from midline in the sagittal plane) using the 1st edition Watson & Paxinos Mouse Brain Atlas ([Watson and Paxinos, 2010](#)).

Whole Transcriptome Microarray

In separate cohorts of adult Amigo2-EGFP male mice (N = 3 mice taken from separate litters), LCM was used mostly as described above to capture the cell body and apical dendritic region from either CA1 or CA2 using different hemispheres from the same mice. In contrast to the methods described above, total RNA was extracted using PicoPure RNA Isolation kit (Arcturus), which yielded a similar concentration of total RNA (5–20ng) but with lower RINs (6.9–7.5). Approximately 5–7 ng of total RNA were amplified as directed in the WT-Ovation Pico RNA Amplification System (Nugen, San Carlos, CA) protocol, sense-strand cDNA target was made using the Nugen Encore Exon Module, and after fragmentation the product was labeled with the Nugen Encore Biotin biotin module. Four micrograms (4.0 μ g) of amplified biotin-cDNAs were fragmented and hybridized to Affymetrix Mouse Transcriptome 1.0 arrays for 18 hours at 45°C in a rotating hybridization oven. Array slides were stained with streptavidin/phycoerythrin utilizing a double-antibody staining procedure and then washed for antibody amplification according to the GeneChip Hybridization, Wash and Stain Kit and user manual following protocol FS450-0004. Arrays were scanned in an Affymetrix Scanner 3000 and the CEL data files were obtained using the GeneChip Command Console software.

RNaseq library construction

cDNA libraries were made using the Ovation Universal RNaseq system for mouse (NuGEN, part # 0348) according to the manufacturer's instructions, including the shearing step to 200bp with a Covaris S-series Sonication System, using 1ng total RNA input for dendrite samples and 5ng total RNA input for cell body samples. The Ovation Universal system affords a number of advantages for working with minimal amounts of total RNA. First, the sample is not depleted of ribosomal RNA (rRNA) prior to first strand synthesis, which minimizes initial loss of RNA yield. Second, the kit uses both random and poly dT primers to ensure partially-degraded RNA, noncoding RNA and mRNA are included in the library. Third, the kit preserves strand information, which enables more accurate determination of isoform-specific expression levels and supports discovery of novel transcripts. Fourth, the increase in library yield afforded by removing rRNA *after* library generation minimizes the number of PCR cycles required for low input samples, thereby decreasing the PCR bias and duplication levels in the libraries (Farris et al., 2017). Samples from each mouse (8 samples/mouse, cell body and dendrite samples from each subregion, CA1, CA2, CA3 and DG) were processed together without the experimenter blind to sample IDs. The resulting cDNA libraries were amplified using 16 cycles of PCR prior to quantification using the High Sensitivity DNA kit (Agilent, Cat # 5067-4626) and a 2100 Agilent Bioanalyzer, as well as fluorometrically using Qubit dsDNA HS Assay kit and a Qubit 2.0 Fluorometer (Invitrogen, Thermo Fisher Scientific). Libraries from one animal were eight-plexed and sequenced on one high throughput lane on an Illumina NextSeq 500 instrument acquiring 100 bp paired-ends reads to a depth of 50 million reads per sample (+/- 10 mil). Four samples (out of 24 samples total) had fewer than 60% of paired-end reads mapped, therefore their libraries were remade and four-plexed on an additional lane as described above. The data are available on Gene Expression Omnibus (GEO) GEO: [GSE116343](https://www.ncbi.nlm.nih.gov/geo/query/acc.cgi?acc=GSE116343). All code used for generating the data is available in a summary markdown file at <https://jmw86069.github.io/jampack/farrisSeq.html>. Normalized data can be downloaded in R as a test dataset for the RNaseq visualization suite "Jampack," published as an accompaniment to this article.

RNaseq analyses

All sequence data was evaluated for quality using FASTQC (Andrews, 2010). From each RNaseq library, reads were trimmed using Sickle (v1.33) (Joshi and Fass, 2011), adapters were trimmed using cutadapt (v1.8.1) (Martin, 2011), and only paired reads with a quality score > 20 and a minimum length of 20 bp were aligned to the GENCODE (vM12) gene models and the mm10 mouse genome assembly index using STAR (v2.5.1b) (Dobin et al., 2013) or Salmon (v0.9.1, indexed with kmer size 31) (Patro et al., 2017) with the recommended ENCODE RNaseq parameters (ENCODE Project Consortium, 2012). The four duplicate samples were merged as technical replicates. Differential gene expression was evaluated in R (v3.4.2) using limma (v3.32.2) (Smyth, 2005) and/or DESeq2 (v1.18.1) (Love et al., 2014) with median normalized Salmon counts for detected genes only. Initially for STAR alignment data, strand-specific gene counts were produced using featureCounts (v1.5.1) (Liao et al., 2014) with transcripts flattened per gene from GENCODE (vM12) gene models and differential expression was evaluated using DESeq2. Midway through our analyses, we noticed that our pipeline was not allocating counts correctly to expected transcripts, so we switched to the pseudocount alignment tool, Salmon, because it outperformed our pipeline in discriminating isoform-specific abundance. However, because Salmon maps more low abundance reads, limma proved to be a better tool than DESeq2 to model and normalize the data. The only analyses that use Salmon and DESeq2 are the gene ontology analyses, where we used gene level data filtered for high abundance genes, which is unlikely to be affected by differential expression method. STAR alignment data, specifically the junction spanning read counts, were also used in the sashimi plots to visualize alternative splicing. Differential isoform expression was evaluated in R (v3.4.2) using limma (v3.32.2) (Smyth, 2005) using median normalized Salmon TPMs for genes with two or more detected isoforms.

RNaseq correlation plots and visualization

Median normalized \log_2 RNaseq counts from Salmon were centered by the mean per compartment (cell body or dendrite). Genes were included in downstream gene level analyses ("detected genes") if at least one group median had signal above noise ($\text{rowMax} \geq 7 \log_2$ counts). Transcripts were included in downstream transcript level analyses ("detected transcripts") if at least one group mean had signal above noise ($\text{rowMax} \geq 2 \log_2$ TPM and $\text{rowMax} \geq 5 \log_2$ counts) and a minimum expression of 10% TPM of the highest expressed isoform. TPM values were used for analyses that were dependent on transcript length (3'UTR length, 3'UTR expression and CAI analyses). Correlation heatmaps were generated with the heatmap.3 (v1.1.1) R package

using “ward” as the hierarchical clustering and “euclidean” as the distance method. All correlations are Pearson unless otherwise noted.

Cross-correlation with published datasets and microarray

In a previous study (Farris et al., 2017), we cross correlated CA2 cell body transcriptome data (separate cohort of N = 3 male mice acquired using the same methods described here) with the Hipposeq CA2 transcriptome dataset (GEO: GSE74985, Cembrowski et al., 2016b). The two datasets correlated with an $R = 0.896$ using the average \log_2 counts from genes detected in both datasets, indicating that the majority of genes were highly correlated across datasets (Farris et al., 2017).

Comparisons with the Cajigas dataset (Cajigas et al., 2012) were performed in R using gene IDs provided in the supplemental material for all transcripts identified in CA1 neuropil (11,713; Cajigas Detected) and filtered neuropil transcripts (2,550; Cajigas Filtered). These lists were compared with our list of putative dendritic CA1 RNAs present in both CA1 cell body and dendrite samples $> 0 \log_2$ counts (21,415; Farris Detected) or $\geq 7 \log_2$ counts (10,877; Farris Filtered). Similarly, comparisons with Ainsley et al. (2014) and Nakayama et al. (2017) were performed in R using gene ID lists provided in the supplemental material. We attempted to find Entrez IDs for each gene in order to properly match gene symbols, and we found all but 49 genes in Ainsley and all but 1 gene in Nakayama. These unidentified genes were still included in the analysis.

To ensure that our RNA lists were enriched or de-enriched with genes expressed in cell types present in each compartment (e.g., neuronal gene expression in cell body), we used single cell gene expression data from mouse cortex (<http://www.brainrnaseq.org/>) (Zhang et al., 2014) and created cell enriched gene expression lists for Astrocytes, Neurons, Oligodendrocytes, Microglia and Endothelial cells to compare with our RNA lists. We filtered for expressed genes (FPKM > 1 in at least one cell type), \log_2 transformed the data, and created lists of genes for each cell class that included genes 2-fold greater than the median. Then we performed hypergeometric enrichment to determine which cell classes were overrepresented in each of our RNA lists based on gene expression.

CEL files from the transcriptome array were imported into R and RMA normalized using the Oligos package (v1.42.0) (Carvalho and Irizarry, 2010). Genes present on multiple rows were collapsed to one row by taking the highest intensity value per sample. Group mean \log_2 intensity values were correlated with the Salmon normalized group means from a subset of the RNaseq data (CA1 and CA2 cell body and dendrite samples). Heatmaps were generated as above, centering by either compartment (cell body or dendrite) or platform (RNaseq or Array).

3'UTR length analyses

Using GENCODE annotated 3'UTR lengths per ‘protein coding’ detected transcript, we compared the average 3'UTR length from each gene list.

Alternative splicing analyses

Isoform specific abundances were generated using median normalized TPM from Salmon. Differential isoform expression analyses were done using the diffSplice function in the R package limma (Smyth, 2005) on detected transcripts (\log_2 TPM ≥ 2 and \log_2 counts ≥ 5 and $> 10\%$ of TPM for most abundant isoform). Hits across comparisons were defined as \log_2 fold change of 0.585 and FDR of 0.05. Candidate hits were then evaluated using sashimi plots generated using the R package ‘jampack’.

To determine whether our dendritic RNAs preferentially express ALE-isoforms, we used GENCODE gene models to define proximal and distal ALEs using 3'UTR start sites. Then for transcripts harboring the same proximal or distal 3'UTR, we took the \log_2 sum of the exponentiated TPMs to meld transcripts per 3'UTR. We filtered for detected melded 3'UTR isoforms (defined as above). We identified 1397 detected RNAs with 2 or more 3'UTRs, of which 1242 had 2 3'UTRs and were used for further analysis. Each RNA was centered by the proximal 3'UTR isoform and we compared the relative isoform expression across sample groups and gene lists. Each sample group showed the same trend (distal UTR $>$ proximal UTR), and all samples were plotted to obtain an average per compartment (cell body and dendrite) across gene lists.

Codon adaptation index

Using GENCODE annotated CDS regions, codon adaptation indexes were tabulated for each detected ‘protein coding’ transcript using a mouse-specific codon usage table (Nakamura et al., 2000) and the Seqinr package (Sharp and Li, 1987) in R. Mitochondrial-encoded genes were removed from analyses as mitochondrial ribosomes use mitochondrial-encoded tRNAs that specify different codons than cytoplasmic ribosomes. We found a positive linear relationship between CDS length and average CAI per transcript, so we calculated the percentage of codons with low CAI, defined as CAI ≤ 0.5 , and compared the averages across groups.

Hypergeometric gene ontology enrichment analyses and visualization

Initially using RNA-seq counts and fold changes obtained from STAR/featureCounts and DESeq2, respectively, we filtered for genes well above noise ($\log_2 \geq 9$) in at least one cell body sample to enrich for pyramidal/granule cells genes, and then further filtered for hits from CA2 CA2 cell body and dendrite comparisons that had a fold change of at least $\pm \log_2 0.5$ with a B-H adjusted p value of ≤ 0.05 . Then we took the positive fold change hits (up) and the negative fold change hits (down) from each subregion and compartment comparison with CA2 and performed hypergeometric enrichment using Illumina NextBio software (Kupershmidt et al., 2010) (more recently named BaseSpace Correlation Engine). The top GSEA categories for DE ‘up’ comparisons all had to do with mitochondrial function.

To confirm and further explore these results, we repeated the analyses using the median normalized RNA-seq counts obtained from Salmon and fold changes from DESeq2, and filtered for CA2 hits as described above. Based on our results from NextBio, and our observation that a number of mitochondrial genes were not yet classified into KEGG gene ontology categories, we added the Mitocarta2.0 (total and cerebrum) gene lists (Floyd et al., 2016) to our GSEA enrichment analyses, which we performed using

the mouse transcriptome as background. Using the phyper function in the R base package 'stats', we took the top 10 adjusted p values from each source category (biological process, canonical pathway, cellular compartment, molecular function, and mitocarta2) per comparison. Then we performed hierarchical clustering on the $-\log_{10}$ adjusted p values across all 12 comparisons (up and down) using 'Euclidean' for distance and 'complete' for clustering to identify gene ontologies with similar enrichment across comparisons. To visualize the mitochondrial genes enriched in CA2 cell body and dendrite samples we made a gene-concept network (cnet) plot using the multiCnetPlot function in the R package 'jampack'.

Laser Capture Microdissection for gDNA qPCR

A separate cohort of 6–8 week old Amigo2-EGFP male mice (N = 3 from separate litters) was used to extract genomic DNA for quantification of mtDNA copy number relative to nuclear DNA. From each subfield (CA1, CA2, CA3 & DG), approximately 50 eight-micron thick cryosections were collected from the cell body and apical dendritic regions as described above. Prior to LCM, a few sections were stained with cresyl violet to verify coordinates (Dorsal Hippocampus: 1.00mm to 1.50mm lateral from midline in the sagittal plane) using the 1st edition Watson & Paxinos Mouse Brain Atlas (Watson and Paxinos, 2010). The cell body samples contained 15–16 sections per cap and the dendrite samples contained 7–8 sections per cap. LCM samples were lysed immediately after dissection with 10 μ L of extraction buffer incubated at 65°C for 3 hours (PicoPure DNA Extraction kit, ThermoFisher). Samples were then spun down and proteinase K was inactivated by heating samples to 95°C for 10min. The genomic DNA samples were used directly for qPCR.

Quantification of mtDNA copy number using qPCR

Quantitative PCR was performed using a 7500 Fast RT PCR Instrument (Applied Biosystems) and power SYBR-Green master mix (Applied Biosystems). For the PCR step, reaction volumes of 30 μ L contained 0.5ng of LCM gDNA, 1X power SYBR Green buffer and 500nM of each primer. The primer pairs for *Gapdh* (Accession Number NM_001289726.1) FW: AGAGACAGCCGCATCTTCTTG RV: GGTAACCAGGCGTCCGATAC. The primer pairs for *mtDNA (CytB)* (Furda et al., 2014) FW: CCCAGCTACTACCATCATTC AAGT RV: GATGGTTTGGGAGATTGGTTGATGT. The PCR protocol was done by hot start at 95°C for 10min then denaturing for 15 s at 95°C, annealing for 60 s at 60°C for 40 cycles followed by a melting curve. Under these conditions and using 1ng of control gDNA extracted from whole hippocampus, *Gapdh* reached a relative threshold (CT) at 22 cycles and *mt-CytB* at 20 cycles. All samples were run in triplicate and displayed a single melting point. PCR products were run on an agarose gel to ensure a single reaction product of correct molecular weight (117 bp fragment for *mt-CytB* and 223 bp fragment for *Gapdh*). Differential gene expression was calculated by $2^{-\Delta\Delta CT}$ (*mt-CytB* normalized to *Gapdh*) from N = 3 mice. Results are presented as \log_2 mean values of technical triplicates with standard error of the mean (SEM) referring to biological replicates.

Multiplexed single molecule fluorescent *in situ* hybridization

Brains from adult male and female C57BL/6J mice were embedded in OCT and sectioned in the coronal plane on a cryostat at 20 μ m and processed for single molecule FISH according to the RNAscope Fluorescent Multiplex kit instructions (Advanced Cell Diagnostics, Hayward, CA). The following probes were used with the RNAscope fluorescent multiplex reagent kit: *Rgs14* (Cat #416651), *Pcp4* (Cat #402311), *Pfch2* (Cat #474791), *Ptpn5* (Cat #467451), *Necab2* (Cat #467381), *Rapgef4* (Cat #428851), *Adcy1* (Cat #451241), *Acan* (Cat #439101), *Mcu* (Cat#482661), *Micu1* (Cat#482671), *Gsto1* (Cat#482651), *Reln* (Cat#405981), *Slc1a2* (Cat#441341), *Synpr* (Cat#500961), *Lefty1* (Cat#506381), *C1qa* (Cat#441221), *Cldn5* (Cat#491611), and Mt-D-loop (Cat #466241).

smFISH Image Acquisition and Quantification

All images were acquired on a Zeiss 780 or 880 meta confocal microscope using a 40X oil immersion lens. Acquisition parameters were set using 3plexed negative controls (cDNA probes against bacterial RNAs not present in mouse tissue) in each of the 3 channels (Alexa 488, Atto 550, Atto 647) so that any signal above the level of background was acquired. Area CA2 borders were identified using *Pcp4* or *Rgs14* as molecular markers; areas CA1, CA3 and DG were identified using defined anatomical locations. Each image was autothresholded and particle number was quantified across the entire image (354.25 \times 354.25 μ m) or a square region of interest (ROI, of constant size) over the cell body layer using the analyze particle function in Fiji (NIH, v2) (Schindelin et al., 2012). The number of nuclei were counted using the DAPI signal. Particle counts per subregion were averaged across sections (typically 2–4 sections per animal) to obtain one value per animal, and data are represented as mean particle count across animals \pm SEM. For the cell body *mtDNA* particle counts, an ROI was loosely drawn around ten DAPI positive nuclei per subregion per image and particle counts were taken as described above. For the dendrite *mtDNA* particle counts, a 60 μ m² ROI was placed in stratum radiatum and particle counts were taken as described above. All statistical analyses were carried out using Graphpad PRISM 7 software, and significance was determined using an alpha level of 0.05. The experimenter was unable to be blinded for quantification due to prior knowledge of hippocampal anatomy.

Immunofluorescence

Forty μ m thick vibratome-cut brain sections from perfused adult male and female C57BL/6J mice were rinsed in PBS and blocked for at least 1 hour in 5% Normal Goat Serum (NGS)/0.3% Triton-100x. Sections were incubated in the following primary antibodies: mouse anti-RGS14 (UC Davis/NIH NeuroMab Facility, AB_2179931, RRID:AB_10698026, 1:1000), mouse anti-STEP (Cell

Signaling, #4817, RRID:AB_2173544, 1:500), rabbit anti-PCP4 (Santa Cruz Biotechnology, sc-74186, 1:500), mouse anti-pyruvate dehydrogenase E1 (Cell Signaling, AB110333, RRID:AB_10862029, 1:1000), rabbit anti-EFCBP2 (NECAB2) (Novus Biologicals, NBP1-84002, RRID:AB_11028373, 1:500), rabbit anti-COXIV (Synaptic Systems, 298 003, RRID:AB_2620042, 1:500). Antibodies were diluted in blocking solution and sections were incubated for 16-20 hours. After several rinses in PBS-T (0.3% Triton-100x), sections were incubated in secondary antibodies (Alexa goat anti-mouse 488 and Alexa goat anti-rabbit 568, Invitrogen, 1:500) for 2 hours. Finally, sections were washed in PBS-T and mounted under Vectashield fluorescence media with DAPI (Vector Laboratories).

In vivo measurement of superoxide production

Adult Amigo2-EGFP male mice were randomized into two groups (5-6 mice per group) and given two intraperitoneal injections (IP) of either dihydroethidium (DHE) (ThermoFisherScientific, 27mg/kg in 40% DMSO/Saline, final volume 200ul) (Hu et al., 2006) or vehicle (40% DMSO/saline) 30 minutes apart. Stock DHE (10mg/ml in 100% DMSO) was diluted with saline immediately prior to each IP injection as the compound is not stable over time at room temperature. Due to the color of the DHE solution, the experimenter could not be blind to treatment. After 18-20 hours post second injection, mice were deeply anesthetized with fatal plus (50mg/kg IP) and transcardially perfused with ice-cold 4% paraformaldehyde. Forty micron sections were cut on a vibratome, mounted onto superfrost plus slides and coverslipped using Permount mounting media (Fisher Scientific). Note that fluorescence mounting medias (vectashield, prolong Gold) were not compatible with lasting DHE signal. Images from 4-6 sections per mouse were acquired on a Zeiss epifluorescence microscope, using 561 laser excitation for visualizing DHE (Tollefson et al., 2003). Vehicle treated animals were used to measure background fluorescence levels, as CA2 has greater levels of autofluorescence compared with neighboring subregions.

QUANTIFICATION AND STATISTICAL ANALYSIS

Unless otherwise noted, statistical analyses were carried out using R (v3.40) or Graphpad Prism 7 software, and significance was determined using an alpha level of 0.05. For figures, pairwise statistical comparisons were restricted to CA2 for clarity and brevity, however, full statistics can be found in the supplemental tables. Statistical details of experiments can be found in the figure legends and above methods.

DATA AND CODE AVAILABILITY

The RNA-seq and microarray data files have been deposited in the NCBI GEO under ID code GSE116343. <https://www.ncbi.nlm.nih.gov/geo/query/acc.cgi?acc=GSE116343>.

All the R code and source data used for analyses in this paper is available at: <https://jmw86069.github.io/jampack/farrisSeq.html>.

ADDITIONAL RESOURCES

Public website for splicing data visualization: <http://splicejam.vtc.vt.edu/>.

Public UCSC genome browser track hub link: <https://genome.ucsc.edu/cgi-bin/hgTracks?org=mouse&db=mm10&hubUrl=https://orio.niehs.nih.gov/ucscview/farris/hub.txt&position=chr13:58800000-59150000>.

RNA-seq visualization R package 'Jampack': <https://github.com/jmw86069/jampack>.